SOLAR FLARE EFFECTS OBSERVED OVER JICAMARCA DURING MST-ISR EXPERIMENTS

BY

PABLO MARTIN REYES

THESIS

Submitted in partial fulfillment of the requirements
for the degree of Master of Science in Electrical and Computer Engineering
in the Graduate College of the
University of Illinois at Urbana-Champaign, 2012

Urbana, Illinois

Adviser:

Professor Erhan Kudeki

ABSTRACT

A study of solar flare effects observed at the Jicamarca Radio Observatory (JRO) will be presented. The observations were made while the Jicamarca radar was conducting combined observations in mesosphere-stratosphere-troposphere (MST) and incoherent scatter radar (ISR) modes. Combined MST-ISR campaigns have been conducted at JRO from December 2004 until January 2009 with the purpose of obtaining calibrated radar cross section (RCS) measurements of the coherent echoes of the lower ionosphere using the measured radar cross-section of incoherent scatter (IS) returns from F-region ionosphere and IS theory [*Kudeki and Milla*, 2011; *Milla and Kudeki*, 2011].

The present study focuses on the effects of six solar flare events observed to cause significant changes in the mesosphere and the thermosphere. The largest event in terms of solar X-ray flux intensity was an X17.1 (peak of $17.1 \times 10^{-4}\,\mathrm{W/m^2}$) solar flare that occurred at approximately local noon on September 07, 2005. The second largest event was an X6.6 (peak of $6.6 \times 10^{-4}\,\mathrm{W/m^2}$) solar flare around 13:54 LT on December 06, 2006. The next event was an X5.5 (peak of $5.5 \times 10^{-4}\,\mathrm{W/m^2}$) solar flare around 16:00 LT on September 08, 2005. The next event was an M3.5 (peak of $0.35 \times 10^{-4}\,\mathrm{W/m^2}$) solar flare around 15:15 LT on December 06, 2006. The final two events were both M2.1 (peak of $0.21 \times 10^{-4}\,\mathrm{W/m^2}$) solar flares and occurred at 12:00 and 15:30 LT on September 08, 2005. During these events we observed an enhancement of D-region radar backscatter while F-region IS echoes were suppressed due to D-region absorption. Also, the equatorial electrojet (EEJ) radar backscatter was suppressed. Radar echoes from 150 km region were observed throughout the events but showed an abrupt initial drop in altitude by about 10 to 20 km followed by a slow recovery of 1 to 2 hours. Finally, in the case of the X17.1 and the X6.6 solar flares, 50 MHz solar radio emissions of type III and V were detected.

To my parents Elmer and Ada, my sisters Vero, Vivi, Tati, and Pati, my grandmother Olgui, and my aunt Amelia

ACKNOWLEDGMENTS

I sincerely thank my adviser, Professor Erhan Kudeki, for his comments and reviews of this work, for his guidance and support, and all his teachings. I want to thank my family for their love and support, especially my parents Elmer and Ada for their wise guidance and teachings throughout different stages of my life. I'm very thankful to Erin McKenna, who has been there since I started writing my thesis and has been supporting me all this time. I would like to thank the Jicamarca Radio Observatory (JRO) director, Dr. Jorge L. Chau, and the Instituto Geofísico del Perú (IGP) executive president, Dr. Ronald Woodman, for giving me the opportunity to enter the fascinating world of science by working at JRO. I would also like to thank the scientific staff, engineers, and friends at the JRO in Lima, Perú, from whom I learned so much when I worked there and also for their support during my visits to the observatory: Alejandro Belleza, Francisco Buendía, Angela Calle, Otto Castillo, Gloria Chia (R.I.P.), Percy Cóndor, Luis Condori, Darwin Córdova, Sergio Daly, César De La Jara, Ladislao Durand, Freddy Galindo, Patricia Gonzales, Karim Kuyeng, Jimmy Lau, José Lavado, Sandra Mendieta, Gabriel Michhue, Marco Milla, Victor Quesada, Walter Rojas, Danny Scipion, Óscar Véliz, Gerardo Vera, Fernando Villanueva, Marita Villaverde, Santos Villegas, Ramiro Yanque, Rommel Yaya, and José Zegarra. I also thank all my colleagues in the Remote Sensing and Space Sciences (RSSS) group: Deepanshu Aggarwal, Narayan Chapagain, Tim Duly, Dan Fisher, Tom Gehrels, Mijail Gomez, Levent Gezer, Brian Harding, Yiyi Huang, James Law, Tony Mangognia, Serge Minin, Fabio Vargas, and Madi Zholbaryssov. They all make a very nice work environment. I also thank the people that made possible the acquisition and the maintenance of the data sets of X-ray flux from the GOES satellites, solar radio spectrographs of Sagamore Hill and Palehua, and the magnetometer data from JRO, Huancayo and Piura. Discussions

and collaboration with my colleagues and friends Marco Milla and Ahmed Akgiray were very useful for their contribution to the development of the calibration technique of the MST-ISR experiment. I am also very thankful to the community involved in developing and maintaining the language I use for programming, Python, as well as all the associated libraries: Numpy, Scipy, and Matplotlib.

TABLE OF CONTENTS

LIST OF TABLES

LIST OF FIGURES

CHAPTER 1

INTRODUCTION

The purpose of this thesis is to describe and explain the solar flare effects (SFE) observed during combined mesosphere-stratosphere-troposphere (MST) and incoherent scatter radar (ISR) measurements performed at the Jicamarca Radio Observatory (JRO). JRO (11.95° S, 76.87° W) is an equatorial station located near Lima, Peru, and includes of a suit of radio and optical remote sensing instruments along with its centerpiece facility, a 50 MHz incoherent scatter radar with MW power transmitters and a 300 m by 300 m modular antenna array system [*Ochs*, 1965]. The incoherent scatter radar at Jicamarca is the premier instrument used to probe the equatorial ionosphere worldwide. Jicamarca ISR has the largest power-aperture product in the world in the VHF band. Among the many modes of operation available at JRO, the MST-ISR mode of interest here is a combined procedure to simultaneously monitor the equatorial mesosphere as well as the ionosphere using pulsing sequences tailored for optimal responses from the turbulent mesosphere and quiescent ionosphere. Ionospheric response allows the estimation of electron density of the F-region ionosphere by using a forward model based on incoherent scatter theory [e.g. *Kudeki and Milla*, 2011], which in turn calibrates the mode for mesospheric returns [*Lehmacher et al.*, 2009].

MST-ISR campaigns have been conducted at Jicamarca from December 2004 until January 2009 forming a database of daytime observations from 6 a.m. to 6 p.m. local time for more than 50 days distributed in 12 campaigns of 3 to 11 consecutive days. Normal response of the equatorial upper atmosphere established in MST-ISR experiments were observed to exhibit sudden changes during solar flare events. This thesis offers a study of the solar flare effects detected in the Jicamarca MST-ISR database in conjunction with auxiliary flare data acquired globally with a suite of instruments specifically operated for solar explorations and physics. Our studies will focus on six distinct flare events with different X-ray flux intensities detected on Sept. 7 and 8, 2005, and Dec. 6, 2006. Data sources utilized in the study include, in addition to JRO, the following: solar radio spectrographs (SRS) from solar observatories, JRO digisonde, magnetometers and GOES X-ray flux data.

The thesis is organized as follows: In Chapter 2 we provide a brief overview of pertinent aspects of solar flare and ionosphere physics including ionospheric propagation effects and D-region absorption. Chapter 3 is devoted to brief descriptions of the data sources and the presentation of the pertinent data sets acquired during the flare events. Chapter 4 offers a comparative study of the data presented in Chapter 3. Particular attention is directed to the sequencing of flare related effects noted in available data sets, from initiation to recovery, and possible explanations of the observed effects in terms of ionospheric propagation, D-region absorption, increased ionization, and redistribution of electron density. Further data and analysis results are also presented in this chapter to clarify the sequencing of flare-induced effects and identify their possible explanations. Mesospheric RCS estimates are also presented and discussed. Chapter 5 offers the conclusions of this study, and suggestions for future work.

The main conclusions drawn from the studies described in the following chapters are as follows:

1. An increase in mesospheric radar backscattered power is detected in all the studied events. In all these events new lower D-region layers become visible starting at 60 km of altitude.

2. D-region absorption due to the increased ionization starts having an impact on the ionosphere for solar flares with intensities of at least M3.5. This attenuation has the following effects on the JRO data. The 1-way attenuation of cosmic radiation, the 2-way attenuation of the IS returns power, and the increase in the calibration constants. The increase in the calibration constants is proportional to the increase

in the 2-way attenuation of the IS returns.

3. Effects on the 150-km irregularities become detectable for solar flares with intensities of at least M3.5. Layers seem to be squeezed together as if "pushed" by the solar radiation. The layer echoes descend several kilometers. The drop was about 1 km for the case of the M3.5 flare and 20 km for the case of the X17.1 flare. The vertical $\mathbf{E}\times\mathbf{B}$ drift calculated for the X17.1 case showed a drop from 28 m/s to 10 m/s . This drift is not related with the drop in the physical location of the existing 150-km structures. The vertical Doppler velocities represent a probe for the $\mathbf{E}\times\mathbf{B}$ drift at F-region altitudes (e.g., *Kudeki and Fawcett* [1993]; *Chau and Woodman* [2004]) and the drop indicates a decrease of the eastward electric field $\mathbf{E}$. The drop in electric field intensity might have been due to the rearrangement of electron density caused bye the flare.

4. Equatorial E-region current increases during solar flares of at least M3.5 of intensity. This manifests in the increase of the difference in magnetic field intensity between JRO and Piura (located about 800 km to the north of Lima). Even though the electric field decreases, the increase in electron density causes the Cowling conductivity to increase further more to allow for an enhanced current. In contrast, the equatorial electrojet (EEJ) echoes were suppressed because the electron density profile might no longer exhibit an upward gradient at the E-region as needed for scattering the 50 MHz radiowaves during the daytime (e.g., *Farley* [2009]).

CHAPTER 2

OVERVIEW OF SOLAR FLARE AND IONOSPHERIC PROCESSES

2.1 Solar Flares

Figure 2.1 shows the increase in electromagnetic radiation intensity at frequencies ranging from radiowaves to X-rays followed by energetic charged particles generated during a typical solar flare as a function of time. Excess radiation during flares is generated due to the acceleration of charged particles through magnetic loops in the solar corona as shown in the sketch on the left of Figure 2.2 and is detected when it arrives near Earth and is monitored continuously by several instruments. The X-ray flux is one of the first types of radiation that arrives to Earth during a solar flare event and is therefore used as a way of detecting and classifying the events. Figure 2.3 shows the X-ray flux versus time obtained by a GOES[1] satellite for two consecutive days (September 7 and 8, 2005). The upper, blue line corresponds to the soft X-ray emissions in the $1 - 8\,\text{Å}$ band, and the lower, green line corresponds to soft X-ray in the $0.5 - 3\,\text{Å}$ band. On the same graph upward arrows indicate the start of solar X-ray flare events and downward curved arrows indicate the maximum flux reached during those events with the corresponding classification code that is explained next.

---

[1] GOES is an abbreviation for "geostationary operational environmental satellites".

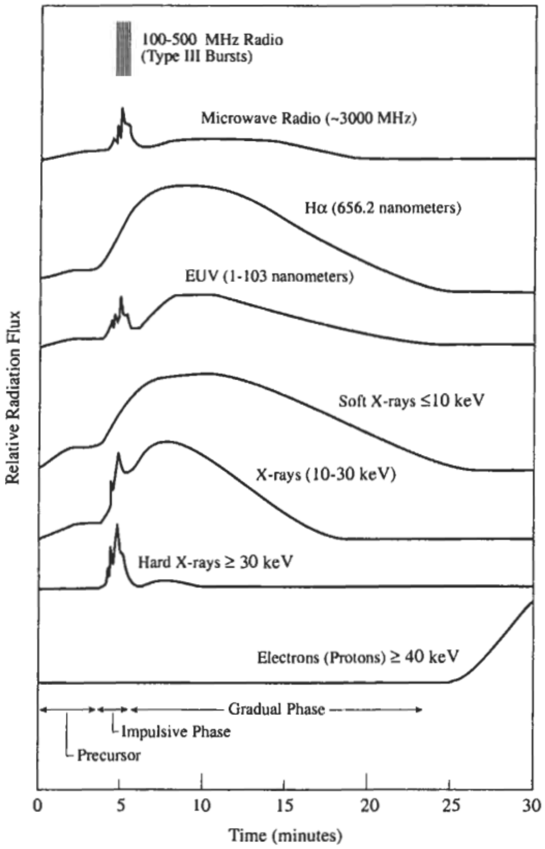

Figure 2.1 – Different types of radiation generated during a solar flare. The sketch shows also that energetic charged particles with energies greater than 40 keV arrive to 1 *AU* (astronomical unit equivalent to 1.49598×10^8 km) 20-30 minutes after the electromagnetic signals. (From *Lang* [2000], adapted from *Kane* [1974].)

2.1.1 Solar X-ray flare classification

According to the NGDC,[2] an X-ray flare is considered to have started when four consecutive 1-minute integrated X-ray values meet the following conditions:

1. All four values exceed the B1 threshold (10^{-7} W/m^2)
2. All four values are strictly increasing.
3. The last value is at least 1.4 times greater than the first value which occurred 3 minutes earlier.

---

[2] The National Geophysical Data Center (NGDC), is a part of the US Department of Commerce (US-DOC), National Oceanic and Atmospheric Administration (NOAA), National Environmental Satellite, Data and Information Service (NESDIS). It provides products and services for geophysical data describing among others the solar-terrestrial environment.

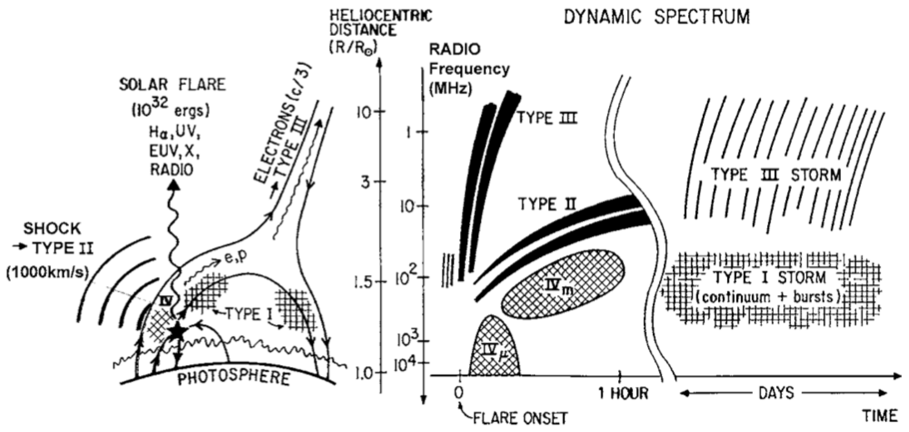

Figure 2.2 – The left side of the figure shows a typical magnetic loop with open magnetic field lines indicating the locations where the different types of radiation are generated. The right side shows the dynamic spectrum of radio events. (From *Bougeret and Pick* [2007].)

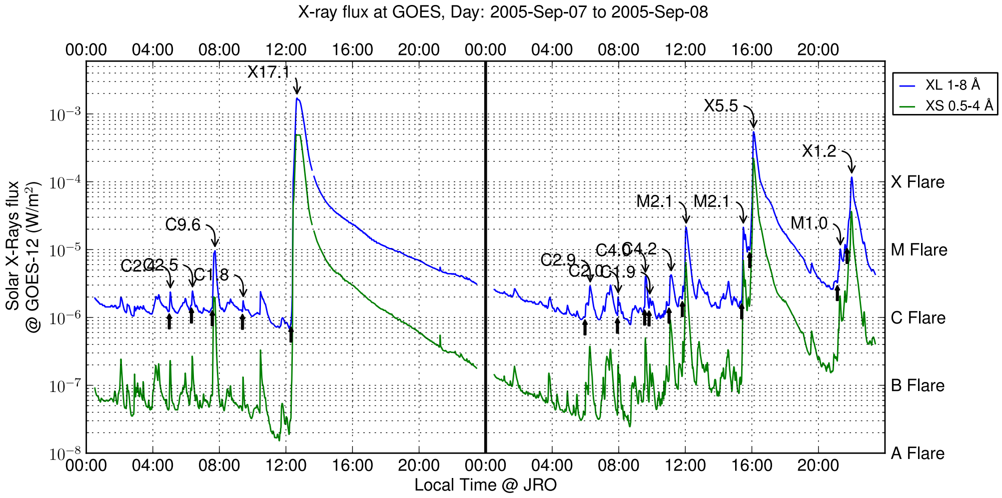

Figure 2.3 – GOES-12 Solar X-ray flux versus time (L.T. at JRO) for days 7 and 8 of September 2005 (1-minute averages). The upper, blue line corresponds to the soft X-ray emissions in the $(1 - 8\,\text{Å})$ band, and the lower, green line corresponds to soft X-ray in the $(0.5 - 3\,\text{Å})$ band. Upward arrows indicate the start of X-ray flare events, and curved downward arrows indicate the classification of the solar flare with its correspondent maximum flux. The data for this plot has been obtained using the NGDC data services.

The event ends when the flux reading drops below half the sum of the maximum and starting flux.

The X-ray flare classification is based on the peak flux in the $1 - 8\,\text{Å}$ band (in W/m^2) detected by the GOES satellites. A letter value (A, B,C,M or X) represents the decadal flux value as shown in the Table 2.1. This letter value is followed by a number indicating the specific intensity of the flare. For example, the flare at approximately 17:30 UT on September 07, 2005, shown in the Figure 2.3 was classified as X17.1, because it had a peak intensity of $17.1 \times 10^{-4}\,\mathrm{W/m^2}$ in the $(1 - 8\,\text{Å})$ band of the soft X-ray emissions.

Table 2.1 – X-ray flare classification (from *Hargreaves* [1992]).

Class	Energy flux in 1-8 Å measured near Earth ($\mathrm{W/m^2}$)
X	$\geqslant 10^{-4}$
M	$10^{-5} \longmapsto 10^{-4}$
C	$10^{-6} \longmapsto 10^{-5}$
B	$10^{-7} \longmapsto 10^{-6}$
A	$10^{-8} \longmapsto 10^{-7}$

2.1.2 Solar radio emissions associated with solar flares

Figure 2.4 shows a sketch of typical solar radio emissions that are generated during a solar flare event as a function of time. The arrow in the time axes indicates the start time of a solar flare, and it is notable that solar radio events or ‘bursts’ can be generated several minutes after the initiation of the solar event. This sketch is similar to the one shown on the right of Figure 2.2, which on the left gives an explanation of the physics related to the different solar emissions.

Solar radio emissions classification

Solar radio bursts have been historically classified into several morphological types [*Wild et al.*, 1963]. Descriptions of the different types of solar bursts and possible explanations of their physics are found in several references [*Bougeret and Pick*, 2007; *Lang*, 2000; *Koskinen*, 2011; *Wild et al.*, 1963; *Cliver*, 2001] from which the summary shown in Table 2.2 has been obtained.

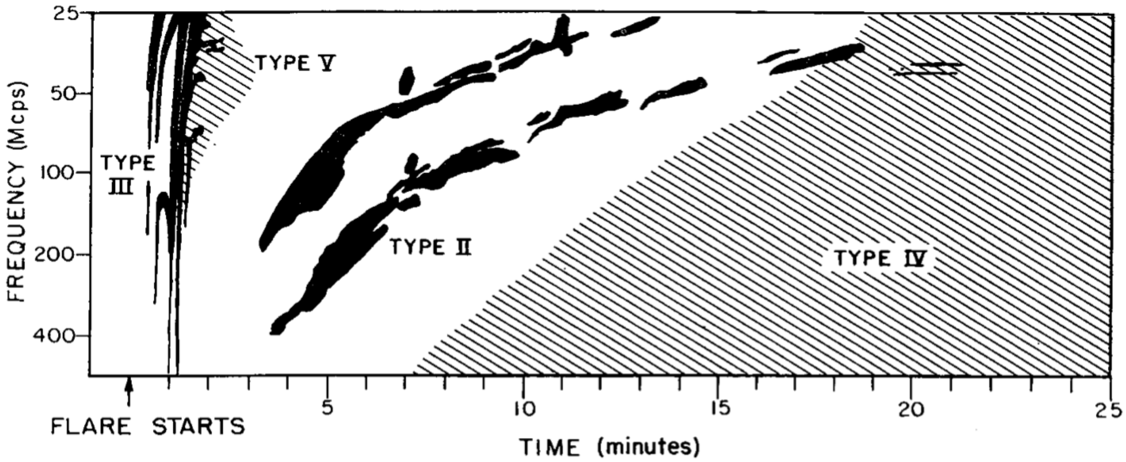

Figure 2.4 – Solar radio emissions associated with a solar flare (from *Cliver* [2001], adapted from *Wild et al.* [1963]).

Table 2.2 – Classification of solar radio emissions during solar flares.

Type	Morphologic description	Source
I	Very short emissions (<1s) appearing in large number forming irregular emission structures.	Generated by electrons accelerated to a few times their thermal energies by energy release in closed coronal loops.
II	Narrow-band emissions at freq. 0.1-100 MHz. Drift slowly to lower frequencies at a rate of about 0.1 - 1 MHz per second.	Outward motion at the speed of about 1000 km/s attributed to outward propagating shock waves.
III	Wide frequency range 10 kHz - 1 GHz. Fast drift from high to low frequencies at a rate of up to 100 MHz per second.	Attributed to beams of electrons thrown out from the Sun by flare process with kinetic energies of $10 - 100$ keV, or velocities up to 0.5 c.
IV	Broad-band continuum radiation lasting for up to one hour after an impulsive flare onset. Partially circularly polarized.	Attributed to gyro synchrotron emission from energetic electrons trapped within magnetic clouds that travel into the interplanetary space with velocities from several hundreds of km/s to about one thousand km/s.
V	Continuum radiation associated with the type III bursts.	Attributed to flare-accelerated electrons moving along open field lines into the corona.

2.2 Earth's Atmosphere and Ionosphere

The Earth's atmosphere is the outermost layer of our planet and consists of molecules and atoms in gaseous form. Figure 2.5 shows the principal layers of the atmosphere using two different metrics to divide it. One of the criteria to divide the atmosphere is the temperature of the neutral gas, which yields to the following four main regions: the troposphere, the stratosphere, the mesosphere, and the thermosphere. The other division criterion is the concentration of free electrons that yields to three distinguishable regions: the D-region, the E-region, and the F-region.

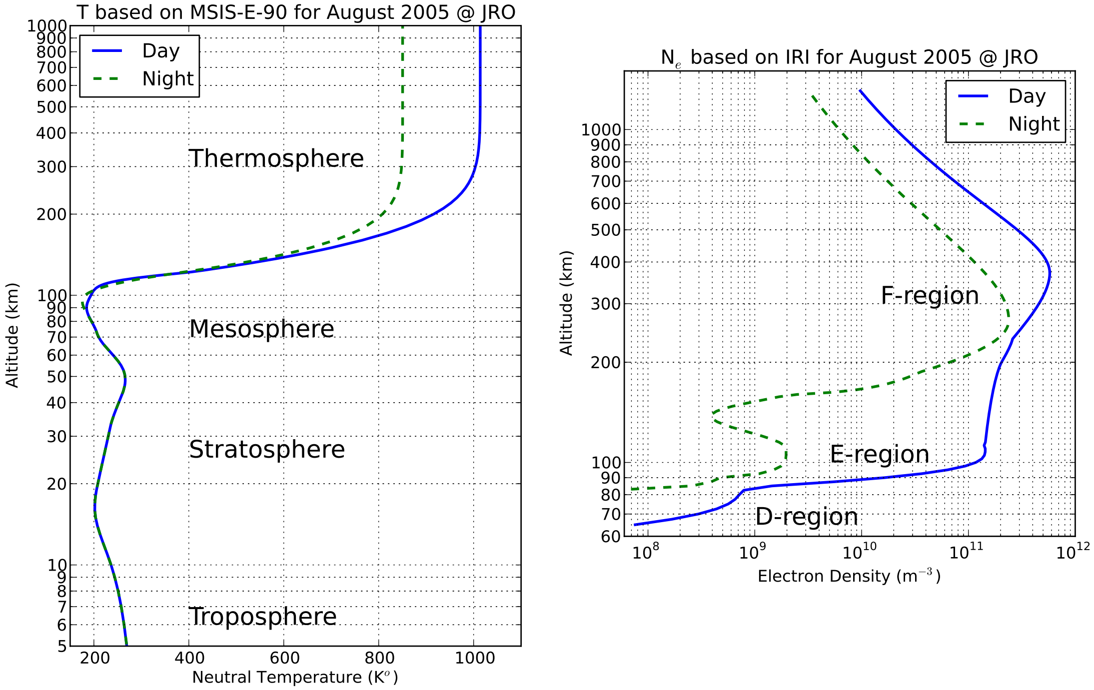

Figure 2.5 – Typical neutral temperature and electron density profile showing the different layers of the atmosphere. These plots were generated with data from the mass spectrometer & incoherent scatter data (MSIS-E 90) model for the temperature profile, and from the international reference ionosphere (IRI) model for the electron density profile. The location chosen was the JRO coordinates, the date August 01, 2005, and the times 0 and 12 local time (LT) for midnight and noon respectively.

The graph on the left of Figure 2.5 shows the division of the atmosphere based on the temperature profile. This plot has been made with data from the mass spectrometer and incoherent scatter data (MSIS-E 90)[3] model [*Hedin*, 1991].

The troposphere is the first layer above the surface of Earth. In this region the temperature decreases with altitude up to the tropopause (around 20 km). The following layer is called the stratosphere and here the temperature increases with altitude up to the stratopause (about 50 km). The mesosphere is the layer above the stratosphere where the temperature decreases up to the mesopause (about 90 km) which is the coldest place in Earth system (average of 190 K). Finally the layer above the mesosphere is called the thermosphere where the temperature increases with altitude up to a maximum of around 1000 K and remains constant in height.

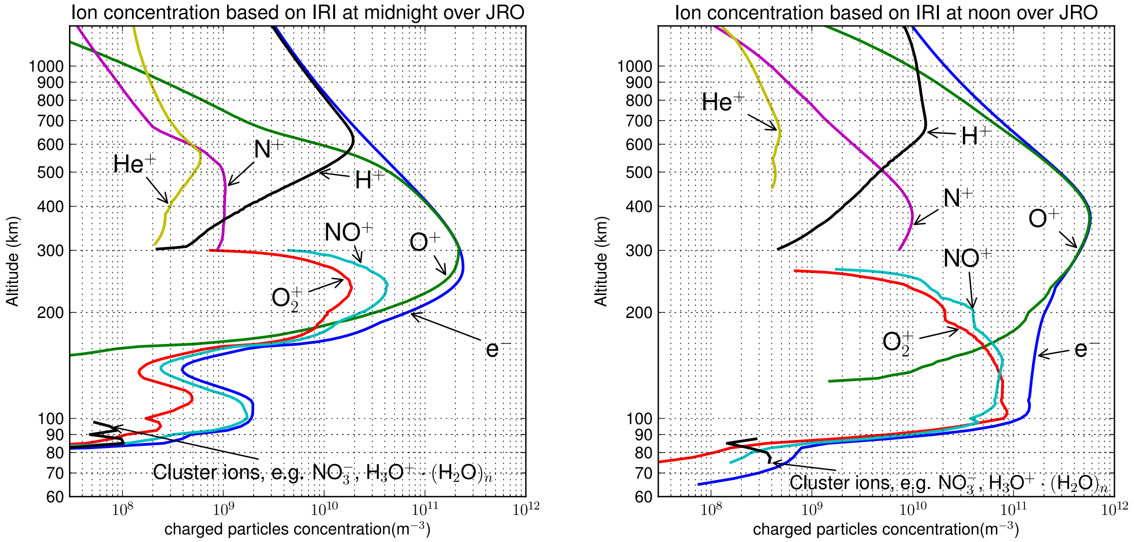

Figure 2.6 – Ion composition plots with data obtained from the international reference ionosphere (IRI) model for the electron density profile. The location chosen was the JRO coordinates, the date was August 01, 2005. The graph on the left represents a sample at midnight and the one on the right at noon.

The part of the upper atmosphere where free electrons and ions coexist with neutral molecules and atoms is called the ionosphere and extends from about 50 km to more than 1000 km of altitude. The graph on the right of Figure 2.5 shows the concentration of free electrons as a function of altitude and indicates the different layers (D, E and F regions) in

---

[3] The MSIS-E model describes the neutral temperature and densities in Earth's atmosphere from ground to thermospheric heights and is based on data compilation from several instruments including incoherent scatter radars. The data can be downloaded online from the following URL : `http://ccmc.gsfc.nasa.gov/modelweb/models/msis_vitmo.php` for a particular location, date and time.

which the ionosphere is divided. This plot has been made with data from the international reference ionosphere (IRI)[4] model [*Bilitza*, 2001].

The ionization of the neutral species in the atmosphere is caused by solar radiation, especially X-ray and ultraviolet radiation that provide the proper amount of energy to an electron bounded to an atom (or molecule) to make it escape from its potential well to yield a free electron and a positively charged ion. Negative charged ions are also present, but only in the D-region where the probability of an electron hitting a neutral molecule and remaining attached to it is larger due to the denser atmosphere.

Table 2.3 – Classification of the ionosphere according to composition (from *Prölss* [2004]).

Name	Range	Main Constituents
D region	$h \lesssim 90\,\mathrm{km}$	e.g. $H_3O^+ \cdot (H_2\mathrm{O})_n$, $\mathrm{N}O_3^-$
E region	$90 \lesssim h \lesssim 170\,\mathrm{km}$	O_2^+, $\mathrm{N}O^+$
F region	$170 \lesssim h \lesssim 1000\,\mathrm{km}$	O^+

A classification of the ionosphere will be done using the ion composition. Figure 2.6 shows two plots of ion composition of the ionosphere versus height for midnight and noon conditions. The data for these plots has been created feeding the IRI model with location and time corresponding to JRO and August 01, 2005. Table 2.3, found in *Prölss* [2004] shows the main constituents found in the D, E and F regions at typical range of altitudes. The F-region is the atomic oxygen ion region; the E-region is dominated by O_2^+ and NO^+; the lowermost region of the ionosphere is the D-region and is where cluster ions and negative ions play an important role. The next subsection is devoted to the D-region in particular the absorption in this layer.

---

[4] The IRI is an empirical standard model of the ionosphere, based on all available data sources (e.g. ionosondes and IS radars) that provides averages of electron density, electron temperature, ion temperature and ion composition for the altitude range from 50 km to 2000 km. The data can be downloaded online from the following URL: `http://omniweb.gsfc.nasa.gov/vitmo/iri_vitmo.html` for a particular location, date and time.

2.2.1 The D-region

The D-region is the lowest part of the ionosphere ($60 - 90$ km) with electron density profile varying from 10^8 to 10^{10} m^{-3}. In this region there are both positive and negative ions. In the E and F regions there are no negative ions, because any free electrons recombine with positive ions more quickly than they can find a neutral molecule to join. In the D-region though, there is a much greater density of neutral molecules so that free electron will be able to collide with a neutral molecule and attach itself to it before it has time to recombine with a positive ion.

As stated in *Hargreaves* [1992] there are six main sources of ionization in the D-region:

1. The Lyman-α line of the solar spectrum (1215 Å) penetrates below 95 km and ionizes nitric oxide (NO).
2. The EUV spectrum between 1027 and 1118 Å ionizes excited oxygen molecules.
3. EUV radiation also ionizes O_2 and N_2 .
4. Hard X-rays of $2 - 8$ Å ionize all constituents, thereby mostly affecting the major species O_2 and N_2.
5. Galactic cosmic rays similarly ionize all constituents.
6. Energetic particles from the Sun or of auroral origin ionize the D-region at high latitudes.

Lyman-α is the major source of ionization below the E-region down to about 70 km, below which cosmic rays are important. Source (2) is less important. The hard X-rays (4) are not important at solar minimum but make a larger contribution at solar maximum when their flux is between a hundred and a thousand times greater.

Absorption in the D-region

As a radio wave travels through a plasma, the collisions between electrons and other particles, mainly neutral atoms and molecules, cause a reduction of its amplitude. This is a result of the conversion of ordered momentum into random or thermal motion. If there were no collisions, the oscillating electron (or ion) would re-radiate all of its energy, which would be restored to the wave. The process of absorption and re-radiation of the energy is accomplished with a change of phase which brings about the change in phase velocity and, hence, of refractive index. In the presence of collisions the ordered motion of the electron is destroyed so that the re-radiated energy is no longer coherent with the advancing wave. Gradually, all of the electromagnetic energy degenerates into thermal energy [*Davies*, 1969].

For calculating the attenuation that a transverse electromagnetic (TEM) wave will experience traveling through the ionosphere, it is necessary to find the effect of collisions in the wave number k. Given a TEM wave propagation in the $+r$ direction, the electric field can be expressed as

$$\mathbf{E} = \mathbf{E}_0 e^{-jkr} = \mathbf{E}_0 e^{k_i r} e^{-jk_r r}, \tag{2.1}$$

where $k = k_r + jk_i = k_o n = \frac{2\pi f n}{c}$ is the wave number, n is the refractive index, and $\mathbf{E}_0$ is the field phasor perpendicular to the traveling direction r. From equation 2.1 the attenuation in dB for every 1000 m travelled by the TEM wave can be expressed as

$$A(k) = 20\,\log_{10}\left(1/e^{\frac{2\pi f}{c} n_i 1000}\right) = -1.8204 \times 10^{-4}\, n_i f\, \frac{\text{dB}}{\text{km}}, \tag{2.2}$$

where $n = n_r + jn_i = \sqrt{1 - j\frac{\sigma}{\omega\epsilon_o}}$ is the refractive index, and f is the carrier frequency. The collisional conductivity σ for a sinusoidal steady-state TEM can be expressed as [*Kudeki*, 2006]

$$\sigma = \frac{\mathbf{J}}{\mathbf{E}} = \frac{Ne^2}{m(j\omega + \nu)} = \frac{Ne^2}{m}\frac{\nu - j\omega}{\nu^2 + \omega^2}, \tag{2.3}$$

where ν is the collision frequency. Using the collisional conductivity and the definition of plasma frequency[5] $\omega_p = 2\pi f_p$, the refractive index formula can be rewritten as

$$n = \sqrt{1 - \frac{f_p^2}{f^2} \frac{1 + j\frac{\nu}{2\pi f}}{1 + \left(\frac{\nu}{2\pi f}\right)^2}}. \tag{2.4}$$

In a partially ionized collisional plasma, such as the ionosphere, electrons will collide with one another, also with neutrals, and with positive and negative ions. But for the lower ionosphere, especially in the D-region, the predominant collision frequency is the one of electrons with neutrals [see *Kudeki*, 2006]. In this regime the electron-neutral collision frequency equation

$$\nu \cong \nu_{en} = 5.4 \times 10^{-16} n_g \sqrt{T}\, \mathrm{s}^{-1}, \tag{2.5}$$

found in [*Rishbeth and Garriott*, 1969], can be used to calculate the electron-neutral collision frequency, where n_g represents the neutral density in m^{-3}, and T the gas temperature in Kelvin.

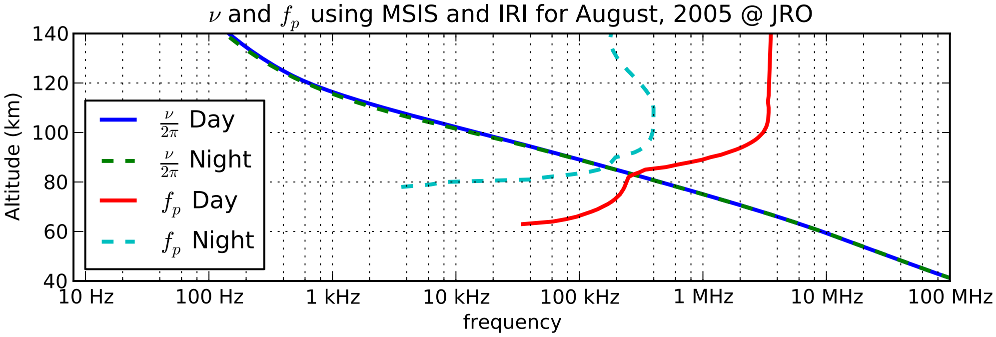

Figure 2.7 – Day and night electron-neutral collision frequency ν_{en} and plasma frequency f_p for an atmosphere under non-disturbed conditions.

Figure 2.7 shows the magnitudes of the electron-neutral collision frequency ν_{en} and the plasma frequency f_p for an atmosphere under non-disturbed conditions. For this plot the neutral density n_g and the neutral temperature T has been obtained from the MSIS-E-90 model. The electron density N_e has been obtained from the IRI model under non-disturbed

---

[5] The plasma frequency ω_p is defined as $\omega_p \equiv \sqrt{\frac{N e^2}{\epsilon_o m}} \approx 2\pi \times \sqrt{80.6N}$, where in IS units, N is the electron density, e is the electric charge, m is the effective mass of the electron, and ϵ_o is the permittivity of free space. This is the frequency at which a volume of electrons will oscillate in a plasma after being moved out from neutral equilibrium (e.g. by an external electric field).

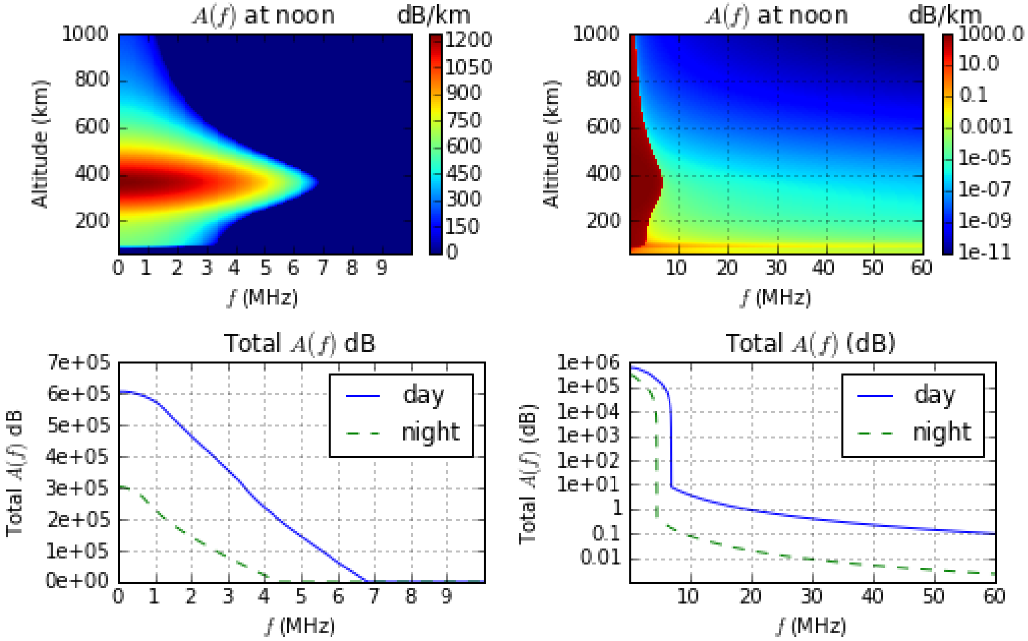

Figure 2.8 – Attenuation $A(f)$ in dB/km and total attenuation in dB for a TEM wave with frequency f traveling through the ionosphere for an atmosphere under non-disturbed conditions at noon.

conditions.

Figure 2.8 shows the attenuation in dB/km calculated using the attenuation formula in equation (2.2) for an atmosphere under non-disturbed conditions. The plots on the left column have been plotted in linear scale and for carrier frequencies less than 10 MHz. The plots on the right column have been plotted using logarithmic scale and for frequencies up to 60 MHz. The plots on the first row show the attenuation in dB/km at every point in frequency and altitude calculated for day conditions. The plots on the second row show the integrated attenuation through the whole ionosphere (0-1000 km) for day and night conditions. For instance, a 50 MHz TEM wave traveling through all the layers of the atmosphere will experience a total attenuation of about 0.1 dB at noon and approximately 0.005 dB at night.

2.3 Sudden Ionospheric Disturbance (SID)

During the occurrence of solar flares, the intensity of solar radiation detected within the ionosphere is increased, and usually is accompanied by radio and X-ray bursts, and occasionally by high-energy particle fluxes. The increase in X-ray radiation is in the order of powers of ten during solar flares, and this enhancement is recognized as the major source of the D-region ionization enhancement during a flare [*Hargreaves*, 1979].

One of the consequences of this increase in the electron density of the D-region is an abnormal ionospheric absorption of high-frequency radio waves. This phenomenon was first discovered by *Dellinger* [1937]. For that reason the phenomenon was known for many years as the Dellinger fade, and is now usually called a “shortwave fadeout” (SWF). Moreover, due to the sudden onset of the fadeout, the immediate effects of solar flares are known collectively as “sudden ionospheric disturbances” (SID).

As discussed in section 2.1, solar flares can be directly measured by ground based and satellite observations. But from the standpoint of the ionosphere and radio propagation, there are a number of terrestrial effects observed which provide information about the flare mechanism. The general classification “sudden ionospheric disturbance”, or SID, includes many of these phenomena which accompany solar flares [*Dellinger*, 1937]. Table 2.4 shows a brief description of SID phenomena occurring nearly simultaneously with the X-ray flare.

Table 2.4 – Classification of sudden ionospheric disturbances (SID) (from *Rishbeth and Garriott* [1969]).

Definition	Description
SWF	Short wave fadeout or “type I” absorption. Waves reflected from the E and F layers are strongly attenuated by enhanced ionization in the D region.
SCNA	Sudden cosmic-noise absorption. A fairly large flare may cause a 2 dB increase in absorption or even more at frequencies of 18 to 25 MHz, which pass completely through the ionosphere without reflection.
SFD	Sudden frequency deviation of signals from a stable HF transmitter, reflected from the E or lower F layers. The deviation is due to a changing phase path, including a lowering of reflection height, as extra ionization is produced.
SPA	Sudden phase anomaly. The phase advance of long waves reflected at oblique incidence indicates a drop of several kilometers in the height of reflection.
SEA	Sudden enhancement of atmospherics recorded at frequencies around 20kHz [e.g. *Bureau*, 1939; *Volland*, 1966]. Atmospherics is referred to the electromagnetic radio waves generated by lightning discharges. Like the SPA, this indicates a change of VLF propagation conditions.
SFE	Solar flare effect or (magnetic) crochet. A disturbance of the geomagnetic field, attributed to increased ionospheric conductivity, which leads to increased current flow.

CHAPTER 3

SOLAR FLARE OBSERVATIONS

On September 7 and 8, 2005, and on December 6, 2006, the Jicamarca radar located near Lima, Peru, made observations of solar flare effects in the D, E and F region ionospheres while operating in the MST-ISR mode. The same solar flare effects were also observed globally using a multitude of instruments and techniques. The solar flare data to be compared and analyzed in this thesis are listed in Table 3.1. This chapter provides brief descriptions of all the instruments listed in Table 3.1 and presents the flare data from these sources to be used in this study.

Table 3.1 – List of instruments and techniques that record the effects of the solar flare.

	Instrument	Brief description of the instrument and the technique used
1	GOES satellite	X-ray sensor (XRS) onboard the GOES satellites.
2	Magnetometers	In situ magnetometers at JRO, Piura and Huancayo, Peru.
3	JRO Digisonde	Digisonde portable sounder (DPS) ionosonde at JRO.
4	SRS	Solar radio spectrograph (SRS) from the solar observatories of Palehua in Hawaii, USA, and Sagamore Hill in Massachusetts, USA.
5	JRO ISR	MST-ISR mode at JRO probing the D, E, and F regions of the ionosphere.

3.1 X-Ray Flux Obtained by the Geostationary Operational Environmental Satellite 12 (GOES-12)

The Figures 3.1, 3.2, and 3.3 show the GOES/SEM[1] X-rays flux, indicating with upward arrows the start times and with downward arrows the solar X-ray flare classification of the events. The plots have been generated using data from the archives held by the National Geophysical Data Center (NGDC).

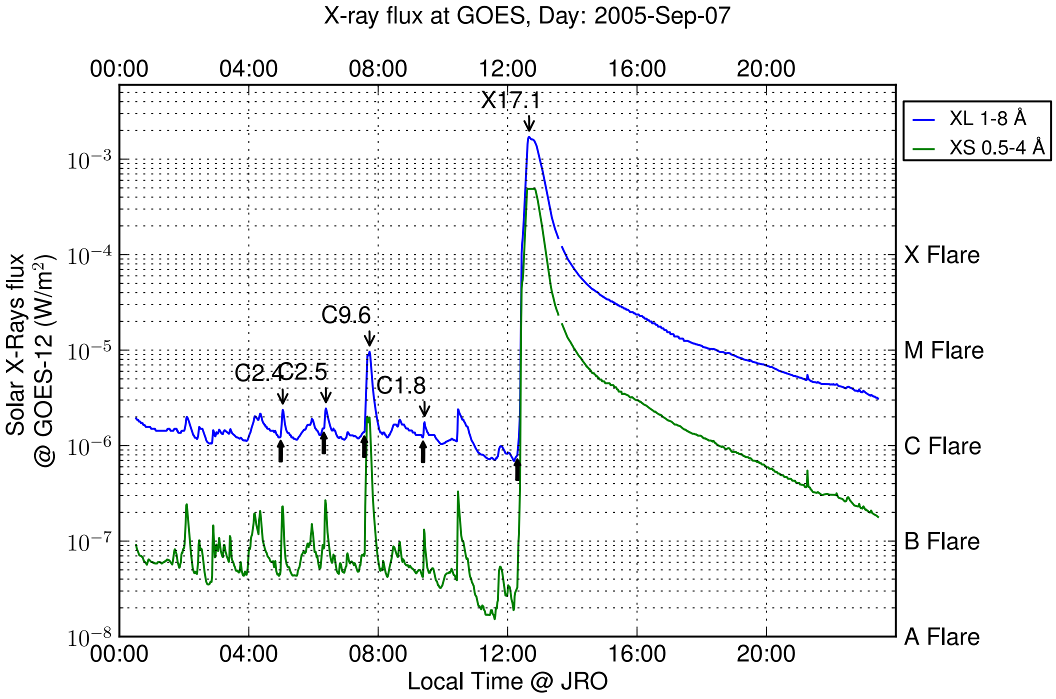

Figure 3.1 – GOES-12 Solar X-ray flux versus time for September 07, 2005 (1-minute averages). The upper, blue line corresponds to soft X-ray emissions in the $(1 - 8\,\text{Å})$ band, and the lower, green line corresponds to soft X-ray emissions in the $(0.5 - 3\,\text{Å})$ band. Upward arrows indicate the start of an X-ray flare event, and downward arrows indicate the classification of the solar flare with its correspondent maximum flux. The data for this plot has been obtained using the NGDC data services.

---

[1] The Geostationary Operational Environmental Satellites (GOES-1, GOES-2, etc.) carry on-board the space environment monitor (SEM) instrument subsystem. SEM system has continuously provided magnetometer, energetic particle, and soft X-ray data since July 1974.

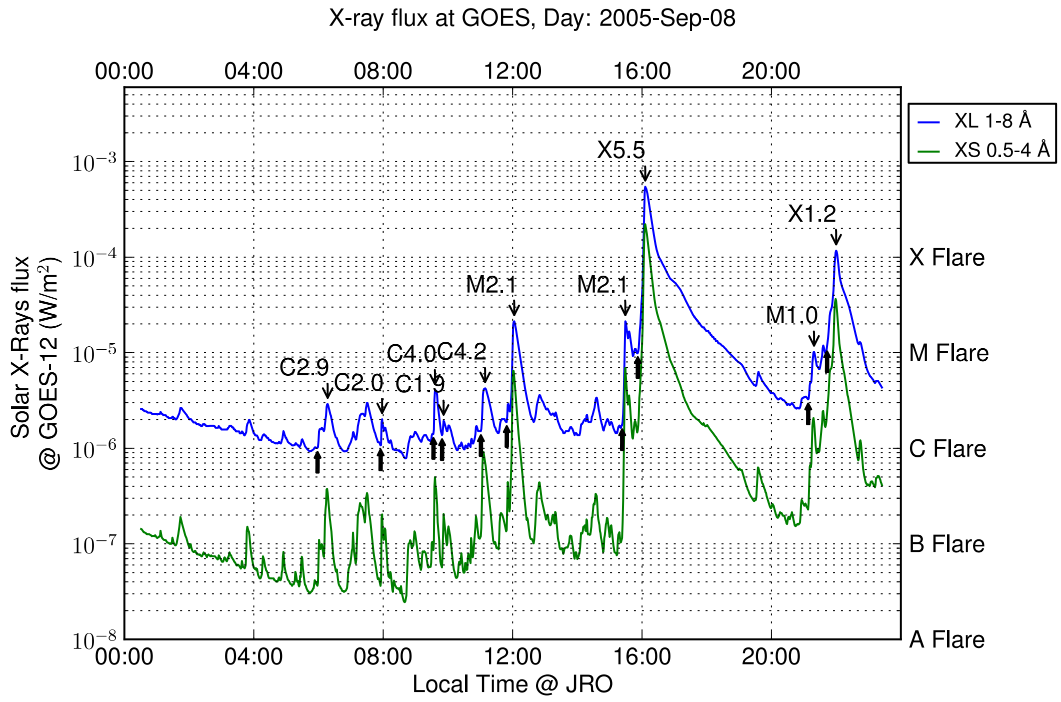

Figure 3.2 – Similar to Figure 3.1 but for September 08, 2005.

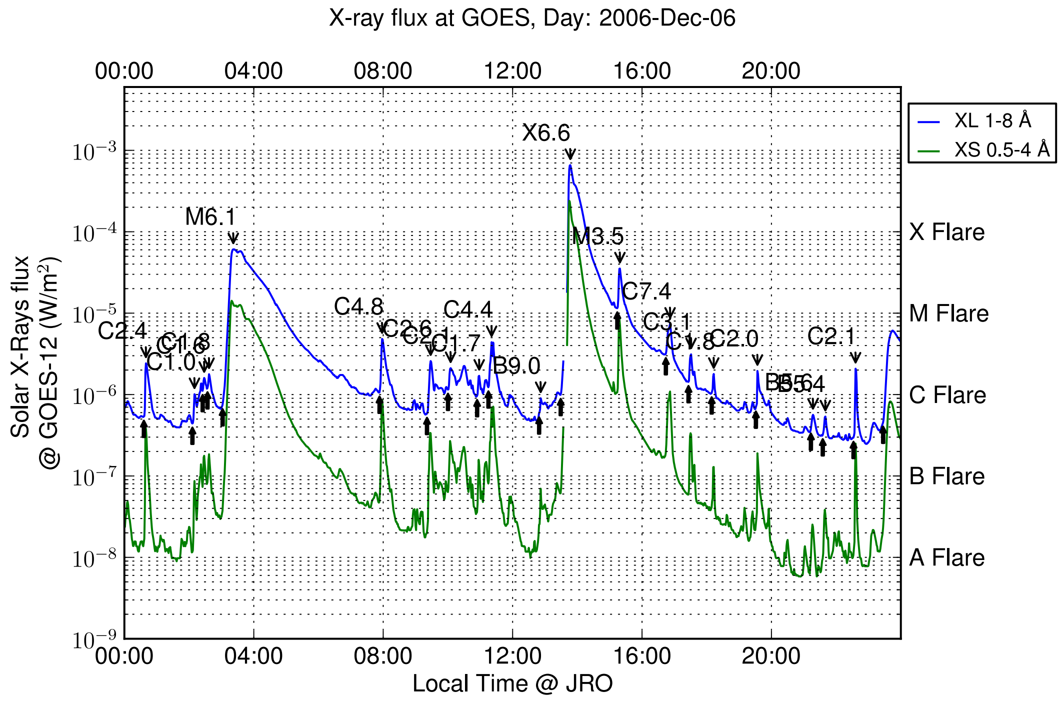

Figure 3.3 – Similar to Figure 3.1 but for December 06, 2006.

Solar X-ray flux data detected by GOES instruments can be monitored in real-time from the NOAA/Space Weather Prediction Center (SWPC) website link for 1 minute averaged data (`http://www.swpc.noaa.gov/rt_plots/xray_1m.html`), and for 5 minute averaged data (`http://www.swpc.noaa.gov/rt_plots/xray_5m.html`). An example of a 5 minute average X-ray flux plot showing 3 consecutive days generated online by the NOAA/ SWPC can be seen in Figure 3.4.

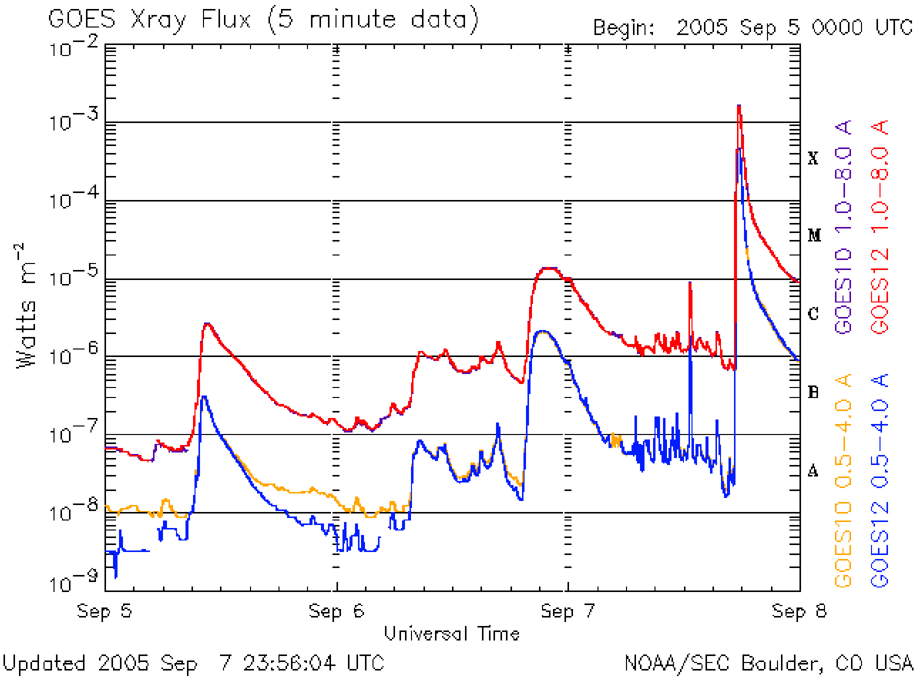

Figure 3.4 – Real time plot of the X-ray flux detected by the X-ray sensor (XRS) at the GOES satellites. This kind of plot is generated in real time by the NOAA / Space Weather Prediction Center (SWPC) .

3.2 Data from Magnetometers

Magnetometers provide a measure of the Earth's magnetic field vector $\vec{B}$ in terms of its horizontal component H, vertical component Z, and declination angle D. The magnetometers at the observatories of JRO, Huancayo and Piura, Peru, are based on the fluxgate[2] magnetometer. Figure 3.5 shows magnetometer data obtained at JRO (downloaded from `http://jro.igp.gob.pe/magnetometers/magnetometers.htm`) on September 07, 2005,

---

[2] The fluxgate magnetometer consists of an arrangement of coils attached to an electronic circuit and can measure the components of the magnetic field directly. A review of this sensor can be found in *Primdahl* [1979].

in which the declination angle is shown in red, H component in blue, and Z component in green. The abrupt increment of the magnetic field intensity around 17:00 UT is known as the magnetic crochet.[3]

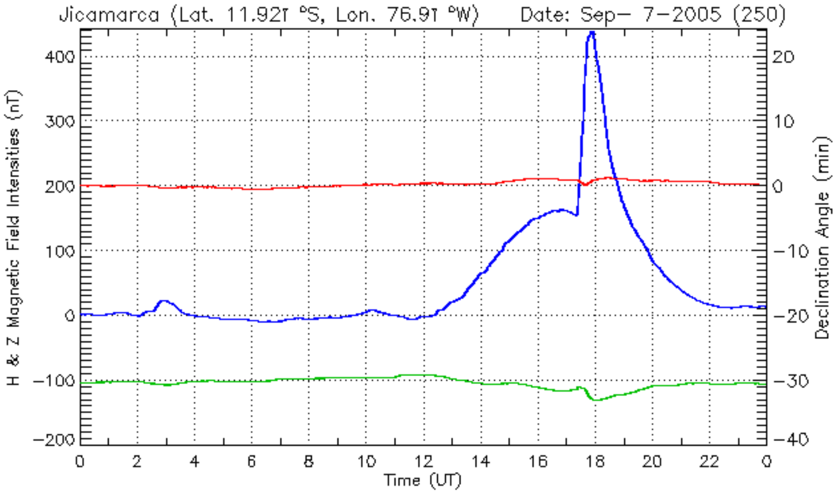

Figure 3.5 – Magnetic field intensity plot measured at Jicamarca on September 07, 2005, showing the magnetic crochet around 17:00 UT. Red is the declination angle (D), blue is the horizontal component (H), and green is the vertical component (Z). This type of graph shows the relative variation of the magnetic field with respect to the mean value obtained at the beginning of the day, and an offset of $-100\,\mathrm{nT}$ has been added to the vertical component, so that it does not superpose to the horizontal component.

A plot of the geomagnetic field components measured at Piura,[4] Peru, is shown in Figure 3.6. The measurements of the two locations are used to produce Figure 3.7, showing the difference between magnetometer measurements at JRO and at Piura, which is used to study the influence of the E-region currents at the magnetic inclination equator.

Figure 3.8 shows magnetometer data obtained at JRO and at Huancayo,[5] Peru on

---

[3] In the event of a solar flare, there is an increase of ionization in the D and E layers of the ionosphere due to the increase in X-ray flux. The enhancement in electron density in the E-layer of the ionosphere causes an increase of the conductivity, which allows for stronger electric currents. At the same time, these electric currents have an effect on the magnetic field. This is detected in the magnetometers as a disturbance showing an increase in the magnetic field intensity and is known as magnetic crochet. This magnetic disturbance was first reported by *Carrington* [1859] in his study of the September 01, 1859, solar flare event. In the case of the solar flare of September 07, 2005, the horizontal component of the earth magnetic field revealed an increase of 300 nT. This magnetic crochet coincides with the increase in X-ray flux due to the solar flare around 17:30 UT.

[4] Piura (5.2° S, 80.64° W) is located in northern Peru, about 800 km north-northwest of Lima.

[5] Huancayo (12.06° S, 75.21° W) is located in central Peru, about 200 km east from Lima.

September 08, 2005. Magnetometer data from Huancayo is provided because there are data gaps in the JRO magnetometer data for that day. The magnetic crochet is visible at the time of the X5.5 flare around 21:00 UT in the Huancayo magnetometer data.

Figure 3.9 shows the variations of the magnetic field intensity measured at JRO on December 06, 2006. The magnetic field was quite variable and a strong excursion is notable at the time of the X6.6 flare around 19:00 UT.

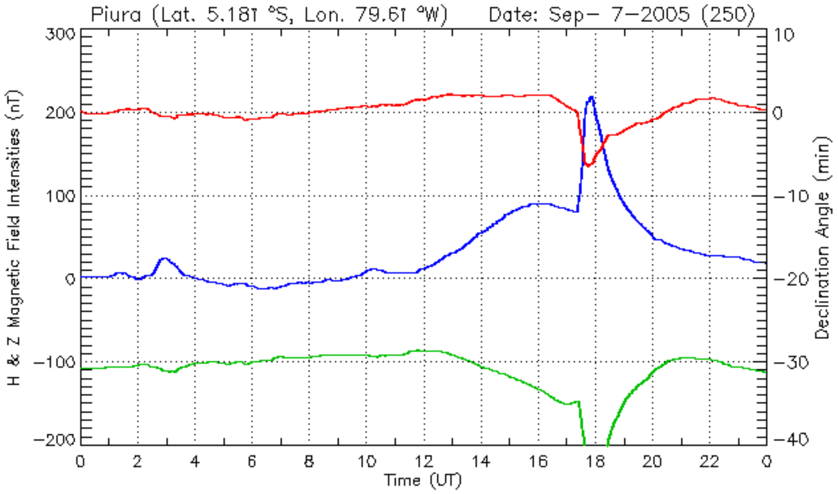

Figure 3.6 – Magnetic field intensity plot similar to Figure 3.5 measured at Piura, Peru (latitude 5.2° south, longitude 80.64° west), on September 07, 2005.

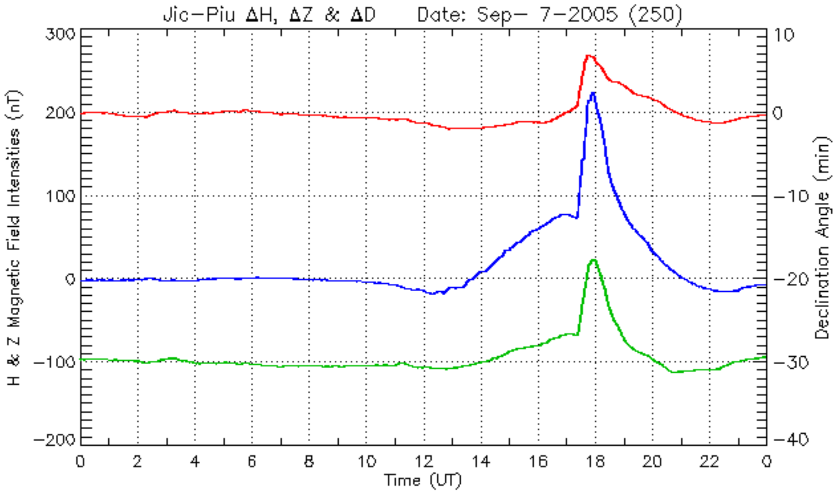

Figure 3.7 – Magnetic field intensity difference plot between JRO and Piura, Peru (latitude 5.2° south, longitude 80.64° west), obtained on September 07, 2005.

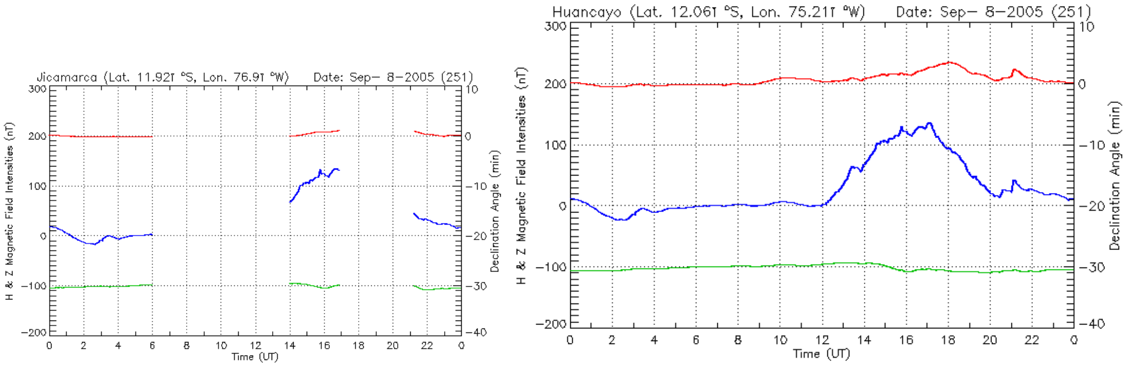

Figure 3.8 – Magnetic field intensity plots similar to Figure 3.5 measured at JRO and at Huancayo, Peru (latitude 12.06 south, longitude 75.21° west), on September 08, 2005 showing the magnetic crochet around 21:00 UT.

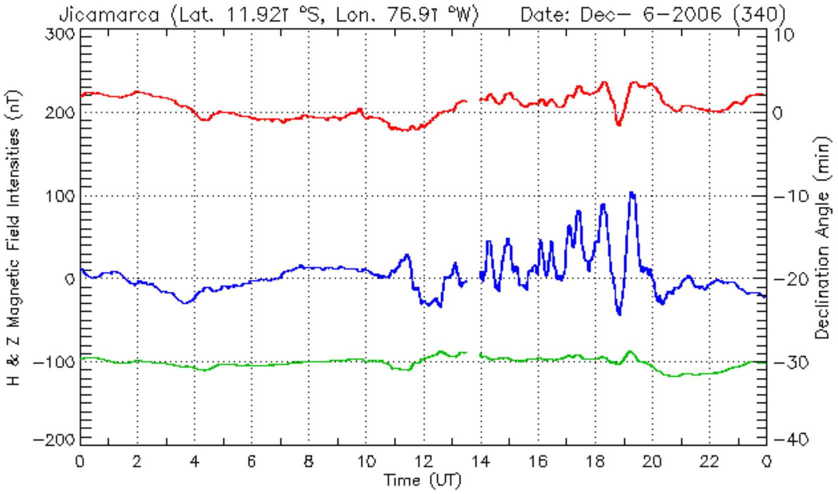

Figure 3.9 – Magnetic field intensity plot similar to Figure 3.5 measured at JRO on December 06, 2006 showing the magnetic crochet around 19:00 UT.

3.3 Ionograms using the Digisonde Portable Sounder (DPS) at Jicamarca

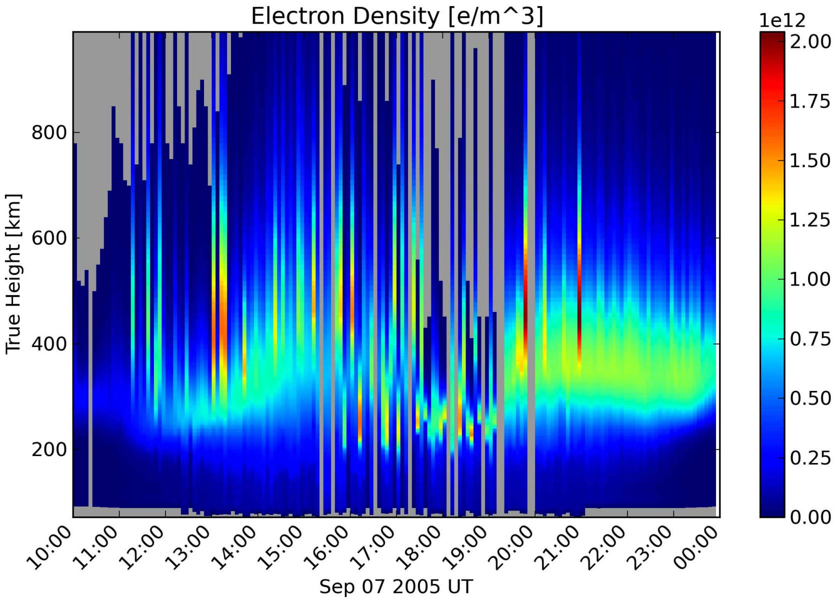

Figure 3.10 – Electron density profiles calculated by the digisonde at JRO on September 07, 2005. The solar flare occurred approximately at 17:00 UT.

Figure 3.10 shows the electron density as a function of height and time on September 07, 2005, constructed using data from the Digisonde,[6] the ionosonde operated at JRO.

Ionosondes operate by probing the ionosphere vertically, sending narrowband pulsed radio waves at different frequencies, ranging from some fraction of 1 MHz up to approx. 20 MHz. At those frequencies, the radio waves experience total reflection at the height where the plasma frequency ω_p equals that of the transmitted radio-wave. The equivalent distance that an electromagnetic wave will travel in vacuum between the time of transmission and the time of reception of the pulsed radio signal is called 'virtual height'. This virtual height is converted into 'true height' taking into account the magneto-ionic propagation effects[7] of the wave traveling through a magnetized plasma like the Earth's ionosphere.

During the MST-ISR campaigns, data from the Digisonde was acquired simultaneously with the radar measurements. In this section, figures are presented with the calculated

---

[6] The Jicamarca Digisonde Portable Sounder (DPS) is an ionosonde developed by the University of Massachusetts Lowell's Center for Atmospheric Research (UMLCAR).

[7] Being the frequency close to the plasma frequency, several slowing down of the wave takes place and two propagation modes coexist: ordinary and extraordinary modes.

profiles of electron density versus the true height during the solar flare events: September 07, 2005 (Figure 3.10); September 08, 2005 (Figure 3.11); and December 06, 2006 (Figure 3.12). The data used was the standard archiving output (SAO) files, obtained from the Digisonde website of the Jicamarca web server: `http://jro.igp.gob.pe/digisonde/digisonde.htm`. For the September 2005 days the Digisonde was acquiring records every 5 minutes, whereas December 2006 it was every 15 minutes. On these plots, the gray color indicates that there is no data available for that particular time and true height.

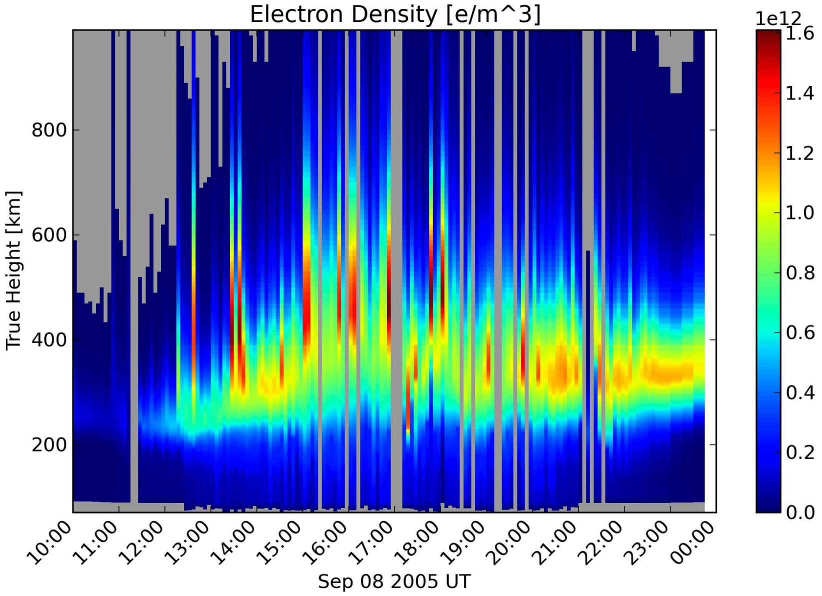

Figure 3.11 – Electron density profiles calculated by the digisonde at Jicamarca on September 08, 2005. The solar flare occurred approximately at 21:00 UT.

On September 07, 2005, an X17.1 X-ray flare event occurred around 17:30 hours UT. Figure 3.10 shows an increase in the electron density at lower altitudes after the solar flare event. Figure 3.11 shows the electron density profiles calculated by the Digisonde software for September 08, 2005. It also indicates an increase in electron density after the increase in X-ray flux starting around 21 hours UT. Finally, Figure 3.12 shows the increase in electron density after the solar flare event around 19 hours UT on December 06, 2006. It is important to notice that the information on electron density given by an ionosonde is only valid until the peak of electron density, since ionosondes are only capable of receiving echo signals up from that altitude.

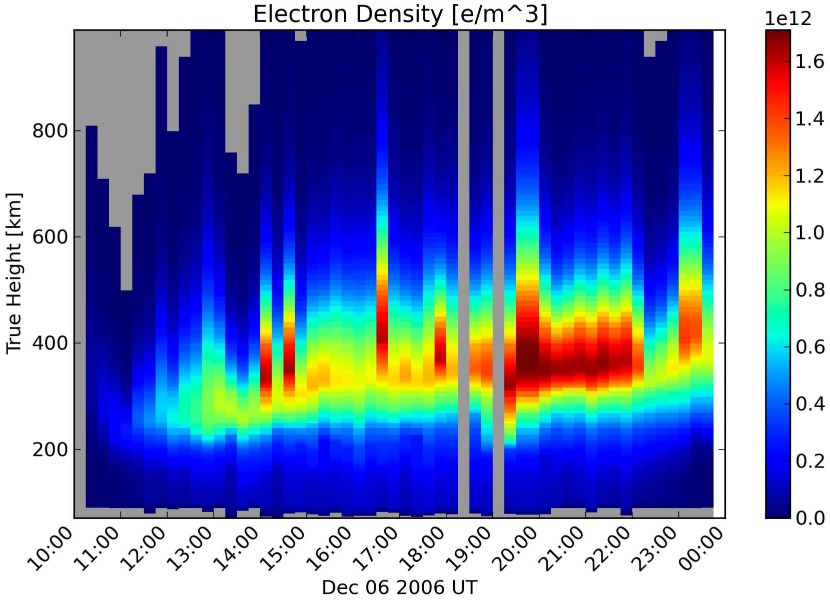

Figure 3.12 – Electron density profiles calculated by the digisonde at Jicamarca on December 06, 2006. The solar flare occurred approximately at 19:00 UT.

3.4 Solar Radio Spectrograph (SRS) Data from Solar Observatories

Figure 3.13 shows a record of a solar radio spectrograph (SRS) obtained on September 07, 2005, at the Sagamore Hill solar observatory. An SRS shows the dynamic spectrum of solar events like the sketches shown in the information given about solar flares in section 2.1. Figures 3.13 and 3.14 show the radio burst generated by the solar flare in the range of 20 to 75 MHz. For comparison with JRO data, Figure 3.14 shows a plot with a 2 MHz bandwidth integrated signal centered around 50 MHz.

In this work data from the ground-based solar observatories of Sagamore Hill, Hamilton, Massachusetts, USA (Longitude: 70.82008°W, Latitude: 42.63225°N) and Palehua, Hawaii, USA (Longitude: 158.11167°W, Latitude: 21.37750°N) will be used. Both observatories are part of the Radio Solar Telescope Network (RSTN) maintained and operated by the U. S. Air Force Weather Agency. A list of other solar observatories can be found in Table 3.2.

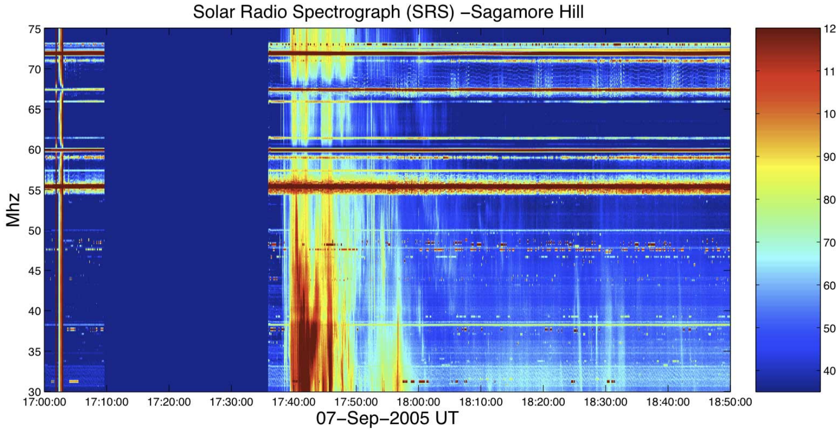

Figure 3.13 – Solar radio spectrograph (SRS) from Sagamore Hill solar observatory obtained on September 07, 2005.

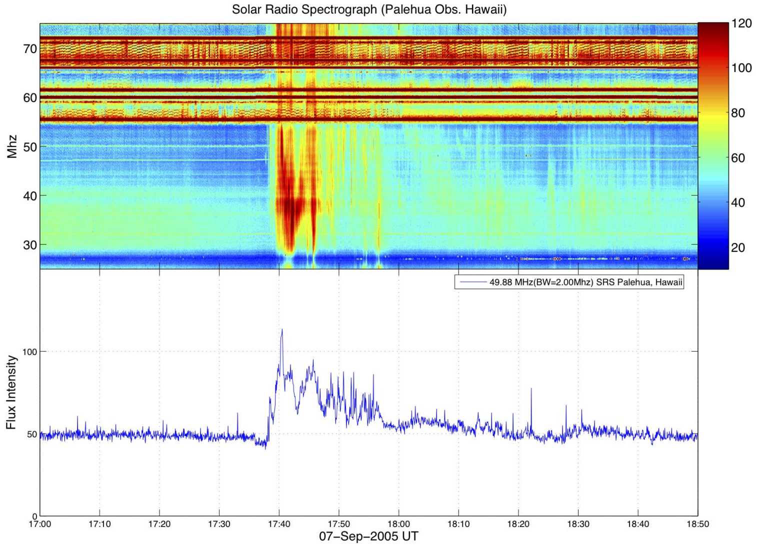

Figure 3.14 – Solar radio spectrograph (SRS) from Palehua solar observatory. In the lower part of the graph the integrated 2 MHz bandwidth, center around 50 MHz solar radiation intensity plot as a function of time is shown.

3.4.1 Data acquisition

The SRS provides measurements within a range of 25 to 180 MHz, completing a whole sweep of this frequency range every 3 seconds. There are two types of antennas used depending on the band scanned. For the low band (or A band), the antenna used is a non-tracking semi-bicone that covers from 25 to 75 MHz. For the high band (or B band), the antenna used is a tracking log-periodic antenna that covers from 75 to 180 MHz. Located at each antenna there is a wide-band preamplifier, and the signal are then fed to a HP8591E spectrum analyzer via coaxial cable. The two spectrum analyzers are connected to a computer (PC) using the GPIB (IEEE-488) bus.

Table 3.2 – Solar observatories abbreviation and locations.

Observatory	Filename abbreviation	Site number	location
Palehua	PA	1	Hawaii, USA
Holloman AFB	HO	2	New Mexico, USA
RAAF Learmonth	LM	3	Western Australia
San Vito Solar Observatory	SV	4	San Vito dei Normanni, Italy
Sagamore Hill Radio Observatory	K7	5	Massachusetts, USA

3.4.2 SRS data

A SRS plot not only shows signals generated in the sun (explained in section 2.1); there are many non-solar signals such as lightning signatures, meteor echoes from FM stations, HF communications from local transmitters and also from long distances (that arrive via ionospheric propagation). Broadcasted signals from TV stations (e.g. Channel 2 at 55.25 MHz with its audio carrier frequency at 59.75 MHz) as well as FM radio stations (88 to 108 MHz) are distinguished as uninterrupted horizontal lines at their carrier frequencies in the SRS plots. Signals from some LEO satellites transmitting continuously in the SRS range and that are close enough to excite the SRS instruments can be seen as horizontal lines that fade in and out as the satellite crosses the horizon. Any other public, military or private communication in the VHF range is seen as broken horizontal lines happening randomly during short amounts of time. One kind of signal that can be interpreted mistakenly as a solar radio burst is the local interference from machinery seen as vertical lines with sharp transitions. Finally, if an ionosonde is operating near an SRS station, the SRS plot will include short horizontal lines increasing in frequency at a constant rate.

3.4.3 SRS plots at the time of solar flares

In days 7 and 8 of September 2005, and December 6, 2006, the SRS plots show evidence of solar radio bursts produced during the solar flares. Figures 3.15-3.20 show the SRS plots during the three solar radio burst events at the observatories of Palehua in Hawaii, and Sagamore Hill in Massachusetts.

Based on the information about solar radio emissions associated with solar flares given in section 2.1 , the radio burst signatures found on these plots match the description given for type III with its associated type V radio emission. According to Table 2.2, the type III emission is characterized with a fast drift from high to low frequencies at a rate of up to 100 MHz per second in the range from 10 kHz to 1 GHz, and those signatures shown in the SRS plots shown in this section also exhibit a fast drift of signals from about 180 MHz to 25 MHz in 1 to 2 minutes. Moreover, based on the sketch of solar radio emissions associated with solar flares shown in Figure 2.4, the type of solar radio burst that matches best the SRS obtained in the days analyzed in this thesis are the type III and V signatures, because of its fast drift across several frequencies in the order or one minute. The associated type V solar emission duration varies for each event, lasting about 7 minutes, 3 minutes, and 15 minutes for September 07 and 08, 2005, and December 06, 2006, respectively.

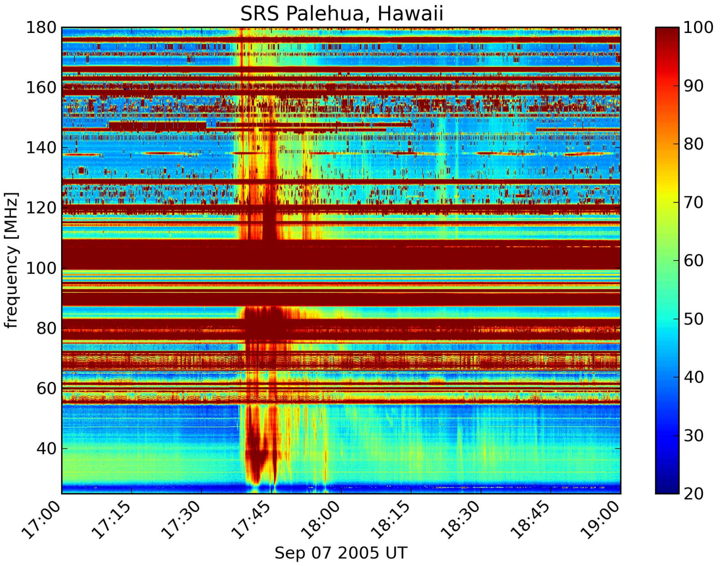

Figure 3.15 – SRS plot showing the solar burst on September 07, 2005, at the observatory of Palehua in Hawaii.

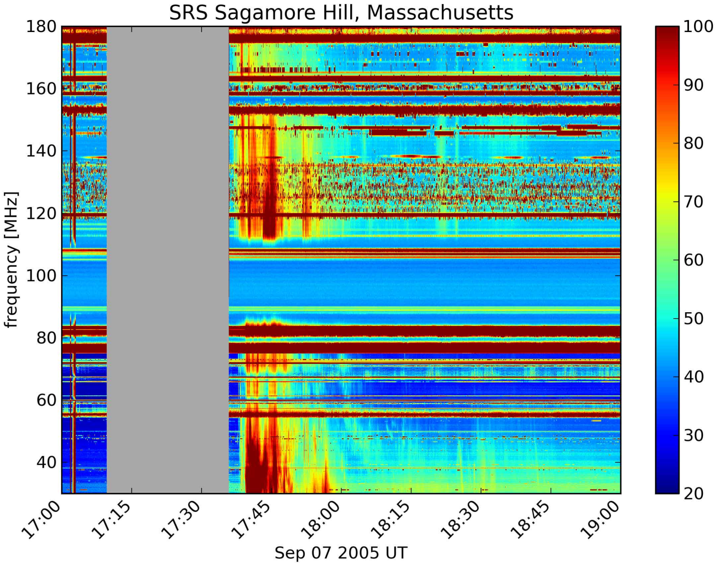

Figure 3.16 – SRS plot showing the solar burst on September 07, 2005, at the observatory of Sagamore Hill in Massachusetts.

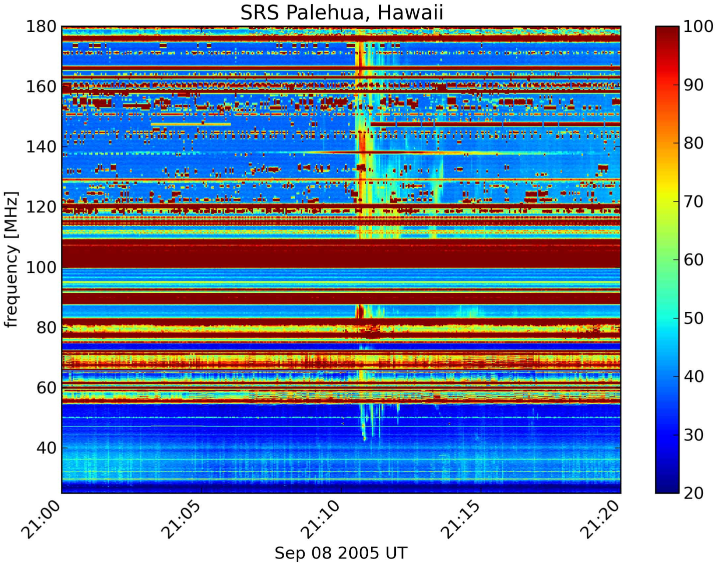

Figure 3.17 – SRS plot showing the solar burst on September 08, 2005, at the observatory of Palehua in Hawaii.

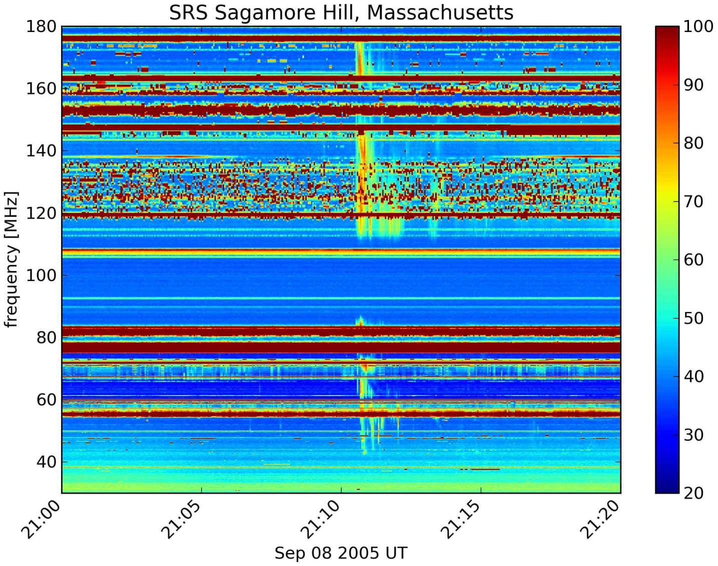

Figure 3.18 – SRS plot showing the solar burst on September 08, 2005, at the observatory of Sagamore Hill in Massachusetts.

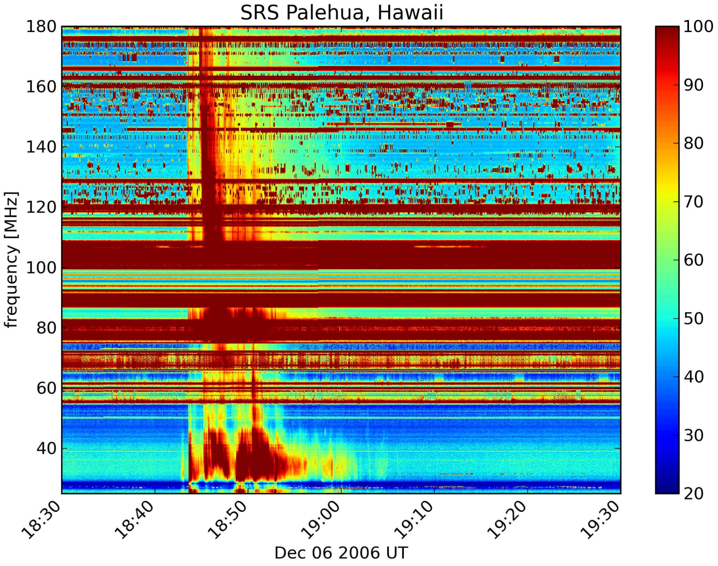

Figure 3.19 – SRS plot showing the solar burst on December 06, 2006, at the observatory of Palehua in Hawaii.

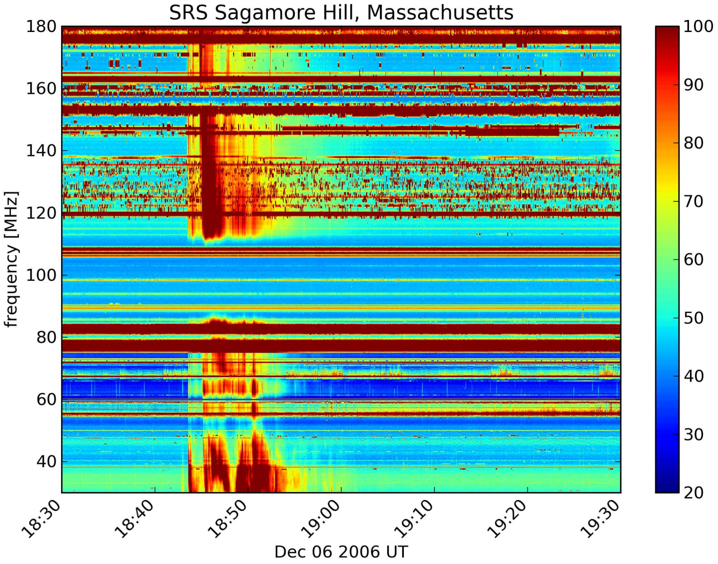

Figure 3.20 – SRS plot showing the solar burst on December 06, 2006, at the observatory of Sagamore Hill in Massachusetts.

3.5 The MST-ISR Experiment at JRO

Figure 3.21 shows a range-time-intensity (RTI) plot of signal-to-noise ratio (SNR) of the backscatter power signal received at JRO during an MST-ISR experiment. In this figure, white text indicates the main detected features in the RTI plot. The IS mode signal is displayed in the top part of the plot from about 200 km to 900 km. It shows IS signal from 200 km to 600 km at 12 LT, and is contaminated by moon echoes around 15 hours LT. The MST mode signal is shown in the lower part of the plot ranging from 0 to 200 km and includes the 150-km irregularities, the equatorial electrojet (EEJ) around 100 km, and mesospheric turbulence around 80 km.

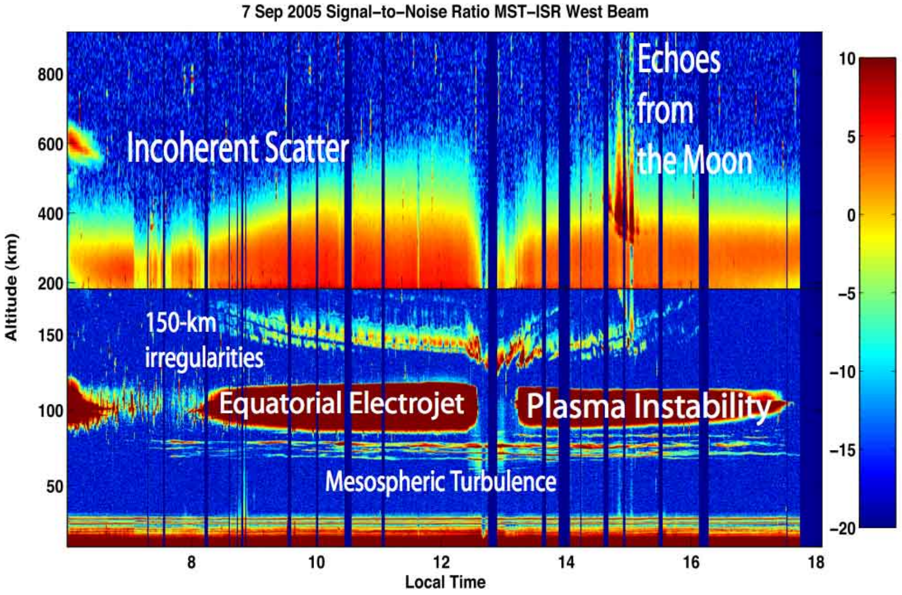

Figure 3.21 – SNR map showing the backscatter power obtained using the antenna beam pointing slightly to the west. This plot shows the IS region from 200 to 900 km, the 150-km echoes region, the equatorial electro-jet (EEJ), an the mesospheric echoes, on September 07, 2005.

3.5.1 Radar parameters and system configuration

The combined MST and ISR measurements are performed in an interleaved way using a set of control pulses consisting of 20 MST pulses followed by 2 ISR pulses as shown in Figure 3.22. The MST pulses are coded with complementary codes of 64 baud and the ISR part uses Barker 3 code. Raw data were recorded for the ISR part, and for the MST part the data was recorded with some processing consisting of decoding and 20 coherent integrations done at the moment of acquisition. The JRO antenna is configured to have four beams, all starting from the center of the main antenna and pointing about 2 degrees off zenith to the North, South, East and West as depicted in Figure 3.23. The 2-way radiation patterns are shown in Figure 3.24.

The sequence of pulses for the combined experiment was obtained by combining two sequences of pulses according with the parameters shown in the Table 3.3. To achieve synchronism with the digisonde (see section 3.3) the system was configured in slave mode waiting for an external pulse every 40 ms (6000 km). The digisonde has a synchronism pulse output with a period of 1000 km (6.66667 ms) that was divided 6 times to have a synchronism pulse of 40 ms that is the length of the combined sequence for the MST-ISR experiment.

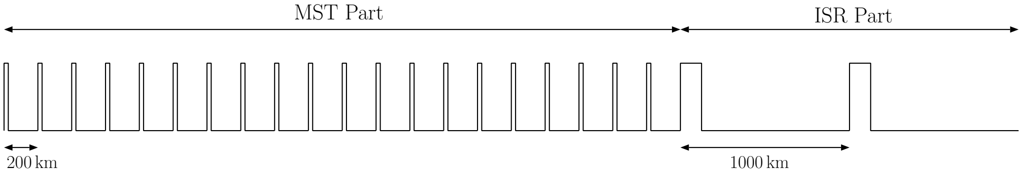

Figure 3.22 – Pulses used in the MST-ISR experiment: 20 pulses for the MST part followed by 2 pulses for the ISR part.

Table 3.3 – Radar operating parameters for the MST-ISR experiment.

Radar parameter	MST	ISR
IPP (Inter-pulse period)	200 km	1000 km
Code	Complementary 64	Barker 3
Transmitted pulse	9.6 km	45 km
Sampling rate	0.15 km	7.5 km
Sampling range	9.6 - 180 km	75 - 925 km
Pre-processing	decoding and 20 coherent integrations	none

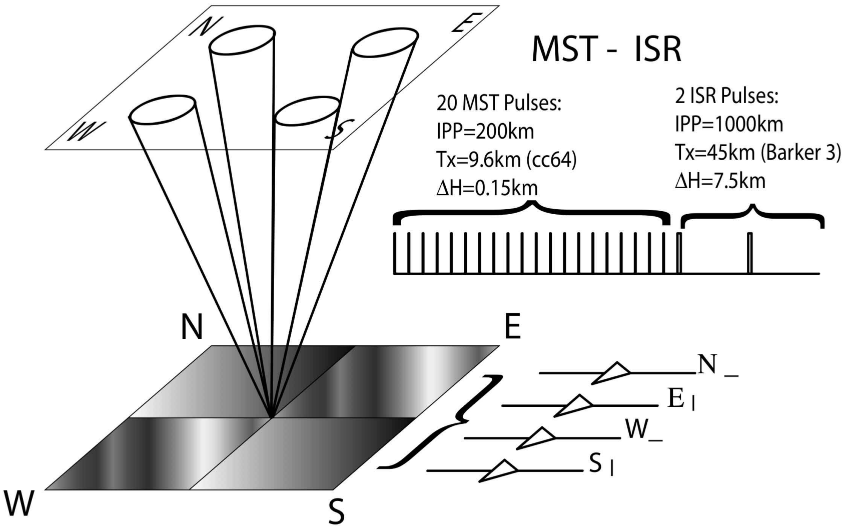

Figure 3.23 – Diagram showing the four antenna beams, their polarization, the experiment parameters and the sequence of pulses for the MST-ISR experiment.

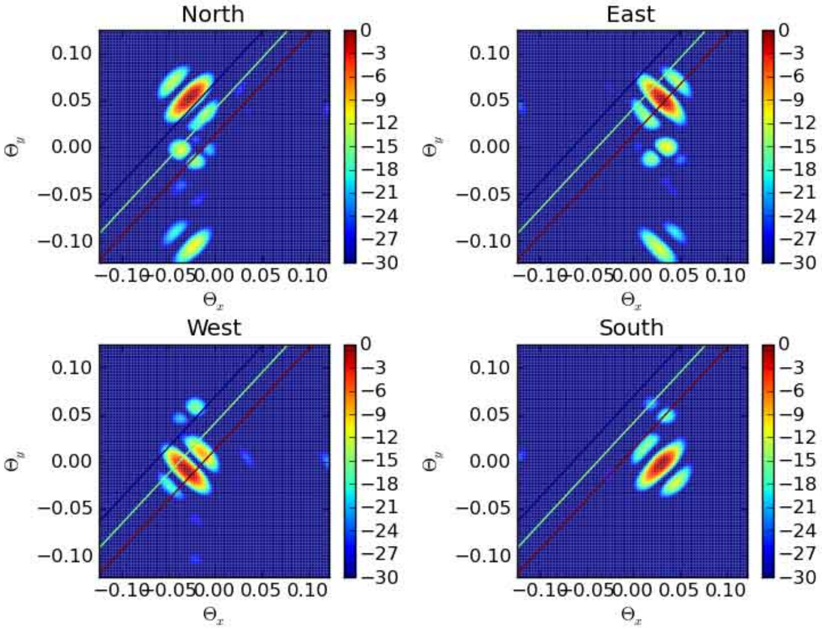

Figure 3.24 – Two-way radiation patterns for the 4 beams used in the MST-ISR experiment. The x and y-axis are the direction cosines θ_x and θ_y . The three straight lines represent the aspect angles 0 and ±1 degrees.

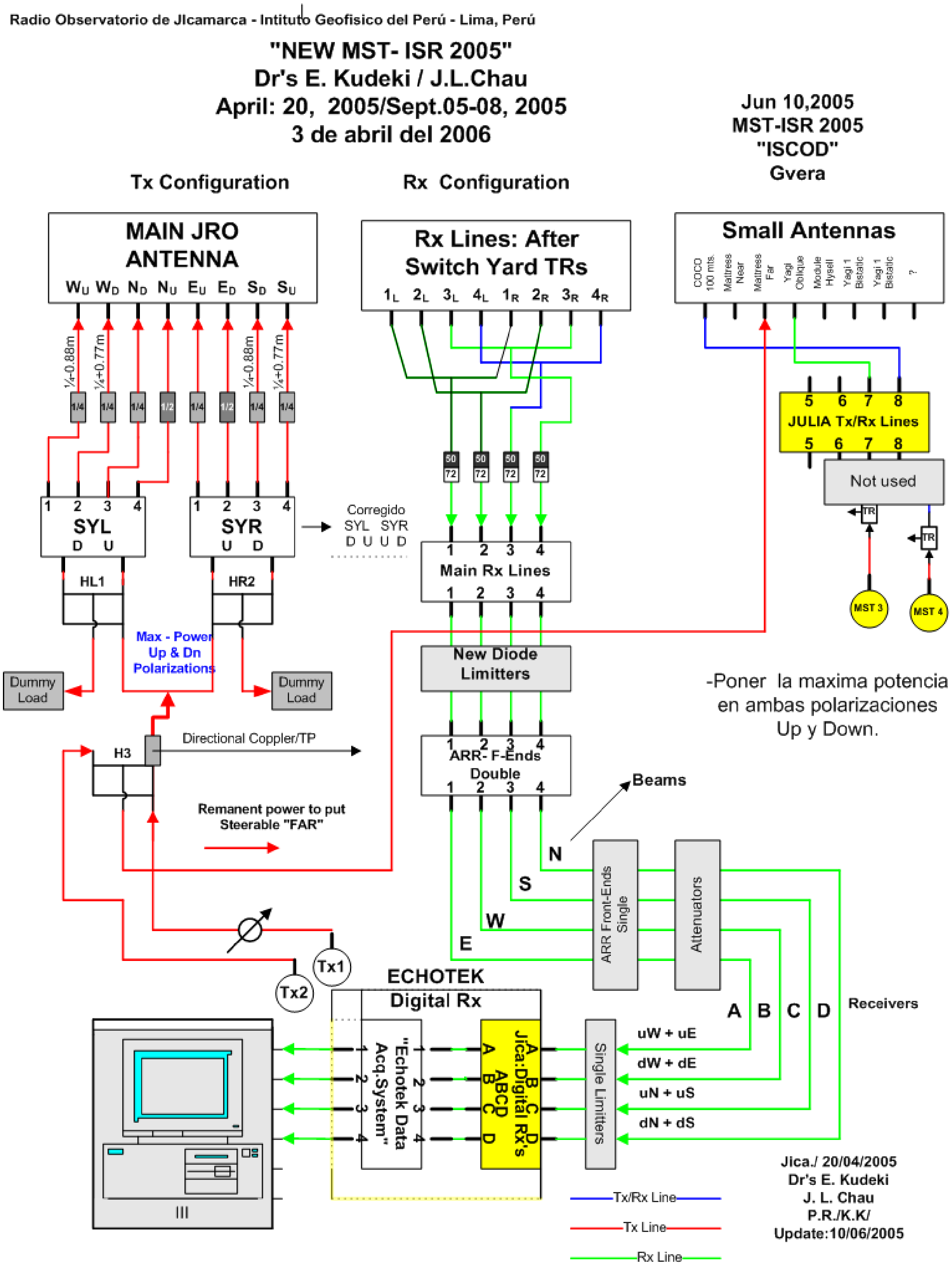

Figure 3.25 – Configuration of the antenna, and the transmitter and receiver transmission lines.

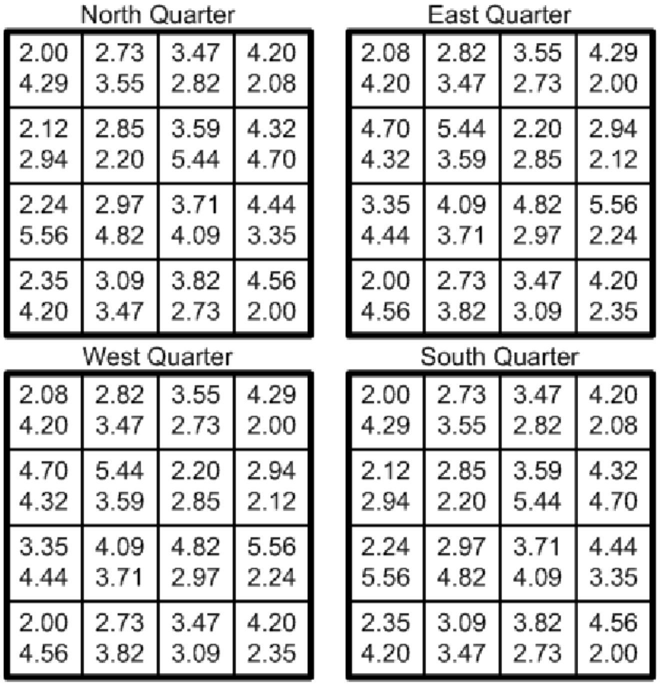

North Quarter

2.00 4.29	2.73 3.55	3.47 2.82	4.20 2.08
2.12 2.94	2.85 2.20	3.59 5.44	4.32 4.70
2.24 5.56	2.97 4.82	3.71 4.09	4.44 3.35
2.35 4.20	3.09 3.47	3.82 2.73	4.56 2.00

East Quarter

2.08 4.20	2.82 3.47	3.55 2.73	4.29 2.00
4.70 4.32	5.44 3.59	2.20 2.85	2.94 2.12
3.35 4.44	4.09 3.71	4.82 2.97	5.56 2.24
2.00 4.56	2.73 3.82	3.47 3.09	4.20 2.35

West Quarter

2.08 4.20	2.82 3.47	3.55 2.73	4.29 2.00
4.70 4.32	5.44 3.59	2.20 2.85	2.94 2.12
3.35 4.44	4.09 3.71	4.82 2.97	5.56 2.24
2.00 4.56	2.73 3.82	3.47 3.09	4.20 2.35

South Quarter

2.00 4.29	2.73 3.55	3.47 2.82	4.20 2.08
2.12 2.94	2.85 2.20	3.59 5.44	4.32 4.70
2.24 5.56	2.97 4.82	3.71 4.09	4.44 3.35
2.35 4.20	3.09 3.47	3.82 2.73	4.56 2.00

Figure 3.26 – Phasing of the antenna. Each small square consists of 12 x 12 half-wave dipoles. This phasing establishes four beam positions with zenith angles of 2.5^o pointing to the four cardinal points (see *Fritts et al.* [1992]).

Two 1 MW transmitters were combined to equally distribute all their power into the 8 antennas (the two cross polarized antennas (Up and Down) of the 4 beams) as shown in Figure 3.25. This is achieved by first combining the two transmitters into one combined line using a directional coupler with a manual control of the phase. The sum of their powers is directed to the main antenna, while the difference is delivered to a secondary antenna, in this case a small "mattress" antenna. Phase is changed until minimizing the power on the mattress antenna, maximizing this way the power to the main antenna. In this scheme, the mattress antenna is effectively a dummy load for dissipation.

Figure 3.26 shows the phasing of the antenna for each of the 64 modules of the antenna array (see *Ochs* [1965]). The two numbers inside each module indicate the phasing cables for the Up and Down cross polarized arrays of dipole antennas. This phasing establishes four beam positions with zenith angles of 2.5^o pointing to the four cardinal points (see *Fritts et al.* [1992]).

3.5.2 Measuring the calibrated radar cross section

In radar measurements, the radar cross section (RCS) represents the backscattering strength of a radar target, and can be defined as

$$\sigma \equiv \lim_{r \to \infty} 4\pi r^2 \frac{S_r}{S_i(\mathbf{r})}, \tag{3.1}$$

where S_r is the backscattered power flux density received by the antenna, and $S_i(\mathbf{r})$ is the power flux density received by the target located at a point $\mathbf{r}$ considering the radar antenna at the origin. The limit indicates far-field approximation. RCS is in units of area and is a magnitude that depends primarily on the characteristics of the observed target. Therefore, measuring the RCS of different targets is an effective way of comparing them. Moreover, measuring RCS is a method of characterizing a particular target in a unique way when using different radars or the same radar with different configurations.

The following derivation will yield to the radar equation for a hard-target which dictates the relation between the transmitted power P_t and the received power P_r in a monostatic radar setup, considering the radar antenna at the origin of a coordinated system and the target located at a point $\mathbf{r}$. The received backscatter power from the target located at $\mathbf{r}$ can be expressed as

$$P_r = S_r A_e(\hat{\mathbf{r}}), \tag{3.2}$$

where S_r is the received power flux density backscattered from the target, $A_e(\hat{\mathbf{r}})$ is the effective area of the receiving antenna for a particular pointing direction $\hat{\mathbf{r}} = \mathbf{r}/|\mathbf{r}|$. The gain of the antenna used by the radar when transmitting can be defined as

$$G_{tr}(\hat{\mathbf{r}}) \equiv \frac{S_i(\mathbf{r})}{S_{iso}(r)} = 4\pi r^2 \frac{S_i(\mathbf{r})}{P_t}, \tag{3.3}$$

where $S_i(\mathbf{r})$ is the incident power flux density at point $\mathbf{r}$, $S_{iso}(r)$ is the isotropic power flux density at a distance r from the antenna, and P_t is the transmitted power. Using the antenna gain definition in (3.3) and the definition of RCS in (3.1), the received power in

(3.2) can be rewritten as

$$P_r = \frac{\sigma S_i(\mathbf{r})}{4\pi r^2} A_e(\hat{\mathbf{r}}) = P_t A_e(\hat{\mathbf{r}}) \frac{G_{tr}(\hat{\mathbf{r}})}{(4\pi r^2)^2} \sigma. \tag{3.4}$$

From antenna theory, the effective area of the receiving antenna is related to the antenna gain in reception as follows:

$$G_{rx}(\hat{\mathbf{r}}) = \frac{4\pi}{\lambda^2} A_e(\hat{\mathbf{r}}), \tag{3.5}$$

where λ is the carrier wavelength. Including this relation in the received power in equation (3.4) yields to the hard-target radar equation

$$P_r = P_t \frac{\lambda^2 G_{tx}(\hat{\mathbf{r}}) G_{rx}(\hat{\mathbf{r}})}{(4\pi)^3 r^4} \sigma. \tag{3.6}$$

The received signal at JRO is a collection of a vast number of scatterers moving randomly inside the observed volume. This collection can be seen as a continuum that can be modeled with infinitesimal volumes $dV = r^2 \sin\theta dr d\theta d\phi$. Each of this volumes behaves like a hard target with a cross section $\sigma_{vt} dV$, where σ_{vt} is the total volumetric RCS. Applying the hard-target radar equation (3.6) for those infinitesimal volumes with random displacements of scatterers leads to a soft-target radar equation of the form

$$\langle P_r(t) \rangle = \int\int dr d\Omega \frac{\lambda^2}{(4\pi)^3} \frac{G_{tr}(\hat{\mathbf{r}}) G_{rx}(\hat{\mathbf{r}})}{r^2} P_t(t - \frac{2r}{c}) \sigma_{vt}, \tag{3.7}$$

where $d\Omega = \sin^2\theta d\theta d\phi$ is the solid angle differential, $2r/c$ is the propagation time delay, and the angular brackets denote the ensemble average (expected value) of the received power. The expected value has been used here because the random displacements of the scatterers defines essentially a random process.

In general, the volumetric RCS depends on the Doppler frequency $\omega/2\pi$, and the Bragg vector $\mathbf{k} = -2k_0\hat{\mathbf{r}} = -4\pi\hat{\mathbf{r}}/\lambda$, so it can be rewritten as

$$\sigma_{vt} = \int \frac{d\omega}{2\pi} \sigma_v(\mathbf{k}, \omega). \tag{3.8}$$

Furthermore, when considering a match-filter receiver, the soft-target Bragg-scatter radar equation generalizes to [*Milla and Kudeki*, 2006]

$$\left\langle |v_i(t)|^2 \right\rangle = E_t K_i \int dr d\Omega \frac{d\omega}{2\pi} \frac{G_{tr}(\hat{\mathbf{r}}) G_{rx}(\hat{\mathbf{r}})}{k^2} \frac{\left|\chi\left(t - \frac{2r}{c}, \omega\right)\right|^2}{4\pi r^2} \sigma_v(\mathbf{k}, \omega), \tag{3.9}$$

where $\left\langle |v_i(t)|^2 \right\rangle$ is the mean square voltage at the output of the i-th receiver, t is the radar delay, E_t is the total energy of the transmitted pulse, K_i is the total calibration constant (K_i accounts for total gain and losses along the i-th path), and

$$\chi(\tau, \omega) \equiv \frac{1}{T} \int dt e^{j\omega t} f(t) f^*(t - \tau) \tag{3.10}$$

is the radar ambiguity function (see *Levanon* [1988]). In equation (3.10), T is the duration of the transmitted pulse waveform $f(t)$.

The significance of the calibration constant K_i can be seen as follows. If at some point during an experiment, the transmitter power decreases, then the calibration constant should also decrease by the same factor. It should be mentioned that the constant K_i is the accumulation of all the losses and gains of the system and throughout the propagation path. D-region absorption can play an important roll in attenuating the 50 MHz signals during extreme X-ray solar flares. These events increase the electron density of the D-region, which increases the attenuation of signals as discussed in section 2.2.1. When doing RCS measurements of the D-region during strong solar X-flares, the calibration constants should be functions of altitude. Essentially, the calibration constants will decrease as a function of altitude accounting for the accumulated attenuation due to D-region absorption. In the following section an altitude dependent calibration parameter will be discussed for different scenarios of electron density profiles.

At JRO the exact amount of transmitted power is unknown and varies upon various factors. For instance, variations in the voltage supplied by the electricity provider will affect the total power transmitted. Also, transmitter tunings are done regularly to get the most amount of transmitted power. Even though the losses in transmission lines can be measured it is not done regularly and remains an unknown. Attenuation during propagation, e.g. D-region absorption, is also an unknown.

Several techniques have been developed to characterize the RCS for the upper ionosphere (F-region) where the dominant scattering process is called the incoherent scatter (IS) (or Thomson scattering) and is well known and understood [*Kudeki and Milla*, 2011; *Milla and Kudeki*, 2011]. The theory of IS is complemented with magneto-ionic propagation effects in radar experiment to obtain accurate measurements of RCS for the F-region.

The D-region has lower ionization and larger neutral density than the F-region and is highly affected by the turbulent neutral winds. In this region, the dominant backscatter process is Bragg scattering due to random fluctuations of the electron density of the order of $\lambda/2$ spacial irregularities caused by the turbulent characteristic of this region. There is no direct relation between the RCS and the backscatter spectrum and propagation effects for the mesospheric region; consequently, the RCS measurements need to be calculated applying estimates for the unknown parameters of the system in the soft-target radar equation.

Woodman and Guillen [1974] described a technique where the RCS calculated for F-region heights was used as a calibrating signal for calculating the mesospheric RCS assuming that the same radar parameters were used for both regions. More recently the MST-ISR experiment was designed to have calibrated RCS measurements of the lower ionosphere using the simultaneously measured RCS of the incoherent scatter signal. This technique is fully described in the master's thesis by *Akgiray* [2007]. Also a review of the theory and implementation is given by *Lehmacher et al.* [2009]. Mesospheric RCS measurements were obtained using this technique and will be shown in Chapter 4.

3.5.3 Altitude dependent calibration constants

As mentioned in the previous section, the calibration parameters K_i represent the total accumulation of gains and losses along the transmit-receive path. Also it was mentioned that if D-region absorption is strong, altitude dependent calibration parameters should be used to obtain correct RCS measurements of the D-region backscatter. As a result of this analysis, we conclude that different electron density profiles will have the same total

2-way attenuation, but will generate different profiles of altitude dependent calibration parameters $K_i(h)$.

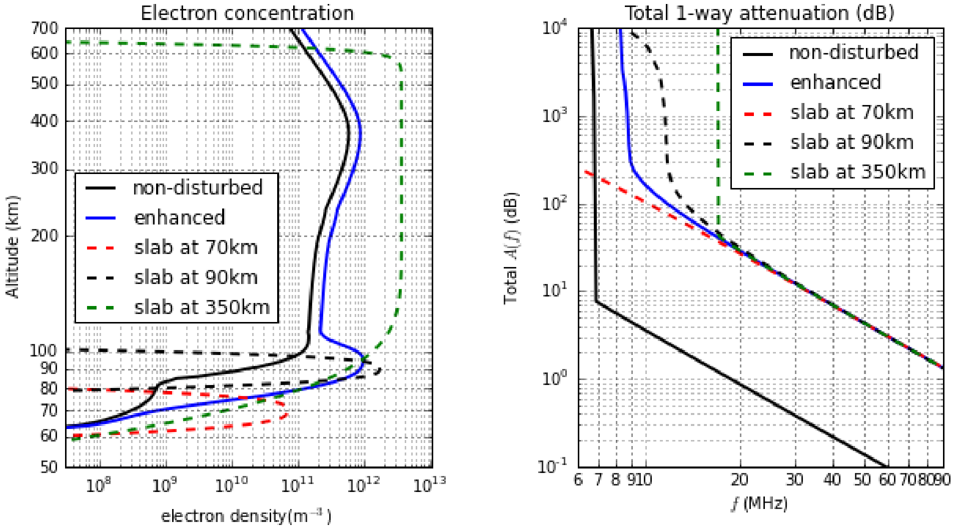

Figure 3.27 – Differences in the total 1-way attenuation suffered by radio signals for disturbed and non-disturbed ionospheres. The enhanced ionospheres have been adjusted such that the total 1-way D-region absorption reaches 4.37 dB of attenuation.

Figure 3.27 shows different electron density profiles on the left and their effect on the total 1-way attenuation on the right. The black solid line represents a typical ionosphere based on data from the IRI model for August 2005 at JRO under non-disturbed conditions and at local noon. The total 1-way attenuation has been obtained integrating the attenuation per unit altitude using

$$\int dhA(h, f), \tag{3.11}$$

where h is the altitude in km, and $A(h, f)$ is the frequency dependent attenuation in dB/km as defined in equation 2.2. The integral of $A(h, f)$ along a path that crosses all ionospheric layers gives us the total 1-way attenuation. The different scenarios of electron density profiles in form of "slabs" has been created using generalized gaussian functions of the form

$$N_e(h) = A\, e^{-\left|\frac{h-h_c}{hw}\right|^p}, \tag{3.12}$$

where A is the amplitude, h_c is the centroid of the slab, h_w is the width, and p is the exponential. Table 3.4 contains the values used for creating the different electron density profiles shown in Figure 3.27. In all the cases, the amplitude A has been obtained by setting total 1-way attenuation at 50 MHz to 4.37 dB. This attenuation was the peak attenuation reached during the X17.1 solar flare based on the maximum variation of the calibration parameters K_i as discussed in subsection 4.1.6. From the total 1-way attenuation in Figure 3.27 we can see that different electron density profiles will experience the same total absorption effect.

Table 3.4 – Formulas used to create different electron density profiles.

	Formula	A (m^{-3})	h_c (km)	h_w (km)	p
normal	$N_{e(IRI)}$ from IRI model	-	-	-	-
enhanced	$1.5 \times N_{e(IRI)} + A\, e^{-\left\|\frac{h-h_c}{h_w}\right\|^p}$	3.61e+12	93	10	2.5
slab at 70 km	$A\, e^{-\left\|\frac{h-h_c}{h_w}\right\|^p}$	6.86e+10	70	5	3
slab at 90 km	$A\, e^{-\left\|\frac{h-h_c}{h_w}\right\|^p}$	1.68e+12	90	5	3
slab at 350 km	$A\, e^{-\left\|\frac{h-h_c}{h_w}\right\|^p}$	3.61e+12	350	250	16

To explore how the calibration constants will change in altitude, we will use the 2-way attenuation. The 2-way attenuation in the D-region is the total attenuation suffered by the backscattered signal in its way up and down to the radar and is calculated using $2\int_0^h dhA(h,f)$. This is twice the accumulation of the 1-way attenuation up to height h and is equal to the ratio in decibels of the calibration parameter at altitude h divided by the calibration parameter without considering the D-region absorption

$$10\,\log_{10}\left(\frac{K_i(h)}{K_{i0}}\right) = 2\int_0^h dhA(h,f), \tag{3.13}$$

where K_{i0} is the calibration constant without accounting for D-region absorption, and $K_i(h)$ is the calibration constant that needs to be used for signals at altitude h.

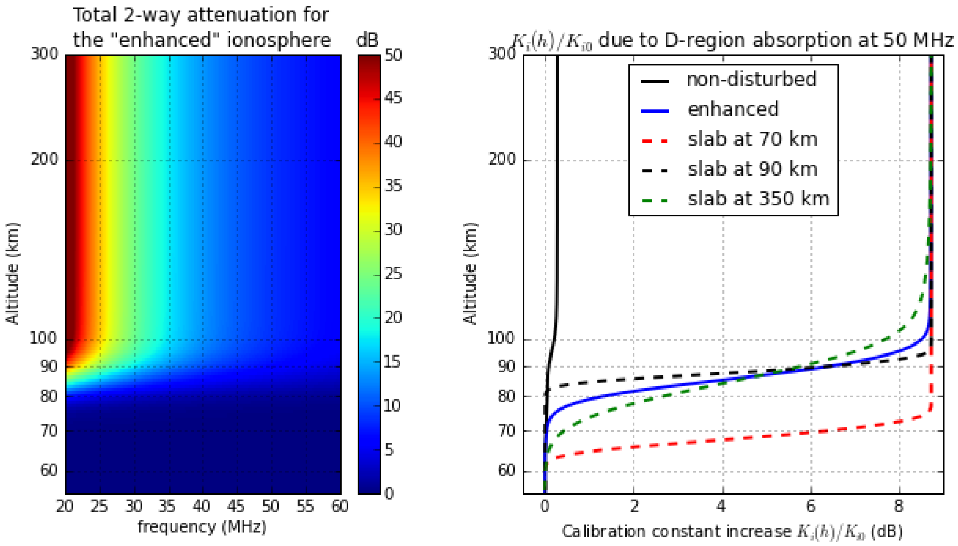

Figure 3.28 – Total 2-way attenuation, and corresponding altitude dependent calibration constants K_i due to a total D-region absorption of 8.75 dB at 50 MHz.

Figure 3.28 shows the 2-way attenuation and the calibration constant increase as a function of altitude. The plot on the left shows the frequency dependent 2-way attenuation for the case of the enhanced ionosphere. The plot on the right shows the altitude dependent increase in calibration constant $(K_i(h)/K_{i0})$ for a carrier frequency of 50 MHz for the different ionospheres depicted in Figure 3.27. From the several curves in Figure 3.28 we conclude that the D-region absorption due to different electron density profiles will generate different profiles of altitude dependent calibration parameters $K_i(h)$.

CHAPTER 4

ANALYSIS AND DISCUSSIONS OF SOLAR FLARE EVENTS

The solar-flare effects (SFE) observed in the data sets discussed in Chapter 3 caused by the major solar-flare events occurring during MST-ISR runs will be shown and analyzed in detail. The events in question are the X17.1 solar flare around noon local time (LT) on September 7, 2005, the X5.5 solar flare around 16 LT on September 8, 2005, and the X6.6 solar flare around 14 LT on December 6, 2006. For each event, JRO data will be shown, described, compared with other instruments, and analyzed in the context of models for propagation and dynamics.

4.1 X17 Solar Flare on Sept. 07, 2005

Figure 4.1 shows a range-time-intensity (RTI) map of the backscatter signal obtained on September 07, 2005, using JRO running in the MST-ISR mode. Sharing the same time axis, the figure also shows on the bottom the X-ray flux detected with the GEOS-12 satellite and on the top an estimate of the background noise at 50 MHz detected at JRO. The RTI map shows the ISR normalized power returns from about 100 to 800 km and the MST mode returns from about 50 to 180 km. The normalized power level in decibels ranges from 6 dB (dark blue) to 16 dB (dark red), except for the region between 85 to 120 km where the power range has been chosen to go from 0 to 80 dB to capture the details of the strong echoes from the equatorial electrojet that otherwise look saturated like in the SNR map of the same day shown in Figure 3.21.

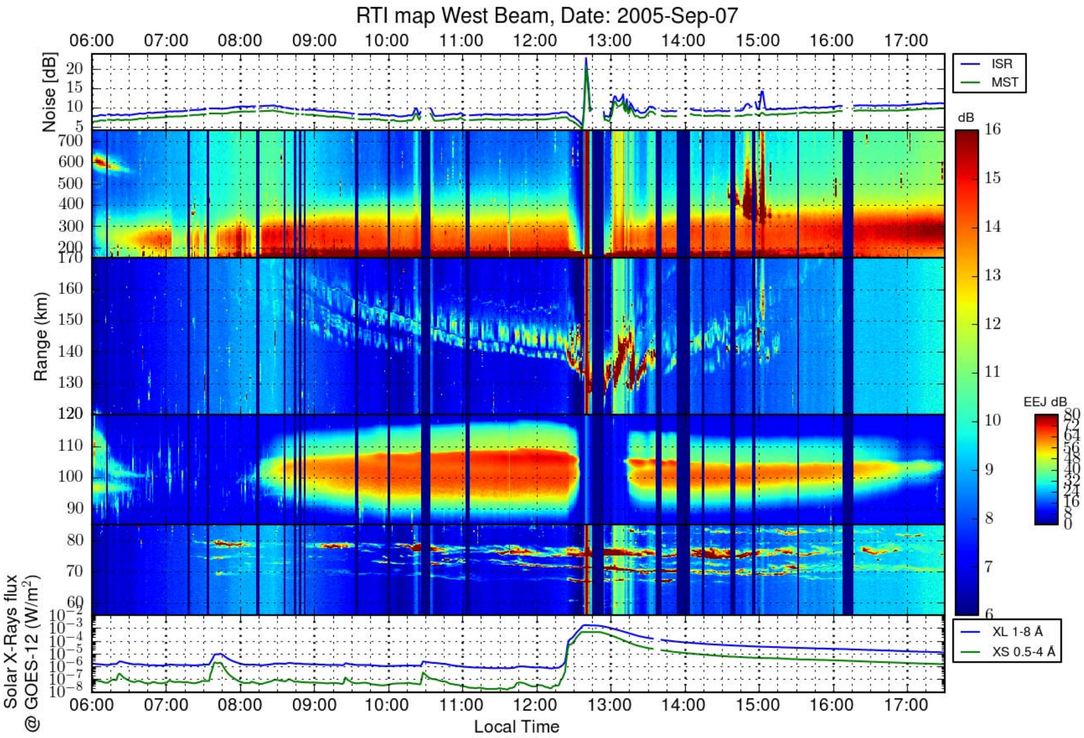

Figure 4.1 – RTI map of the MST and ISR regions in a 60 seconds time resolution during the X17.1 solar flare on September 7, 2005. The plot in the top shows the background noise power for each mode. Incoherent scatter, 150-km irregularities and mesospheric turbulent layers are shown with the dB range (6 to 16 dB) while the equatorial electrojet (EEJ) is shown with a larger dB range (0 to 80 dB) to notice its structure. The plot in the bottom shows the X-ray flux obtained from the GOES satellite.

Notice that the RTI plots contain not only radar backscatter but also radio noise arriving from the cosmic background as well as the sun possibly filtered by ionospheric propagation effects. In that sense, both the scattered radar signal and the background noise constitute signals of interest for this study. That is the reason why we have chosen not to normalize the power by the background noise, as is customarily done in radar signal processing. However later in the chapter we are going to provide the standard signal-to-noise ratio (SNR) plots of the same events.

In the following subsections we focus on a number of details of the observations included in Figure 4.1

4.1.1 Effects on the background noise

Figure 4.2 shows three plots comparing from 12:00 to 13:45 LT at JRO the MST background noise detected at JRO, the solar X-ray flux obtained by the GOES-12 satellite and the averaged solar radio emission at 50 MHz ± 1 MHz received by the solar observatories of Sagamore Hill, Massachusetts, and Palehua, Hawaii. The upper plot shows how the background noise detected at JRO started to drop at 12:25 LT, right after the arrival of the first X-ray flux impulse that reached a flux of approximately 10^{-4} W/m^2 . The cosmic-noise continued to drop slowly for 15 minutes until reaching almost 3 dB of attenuation around 12:37 LT. At that time the solar radio burst at 50 MHz arrived at Earth and the background noise level at JRO, dominated by that radiation, increased by about 15 dB.

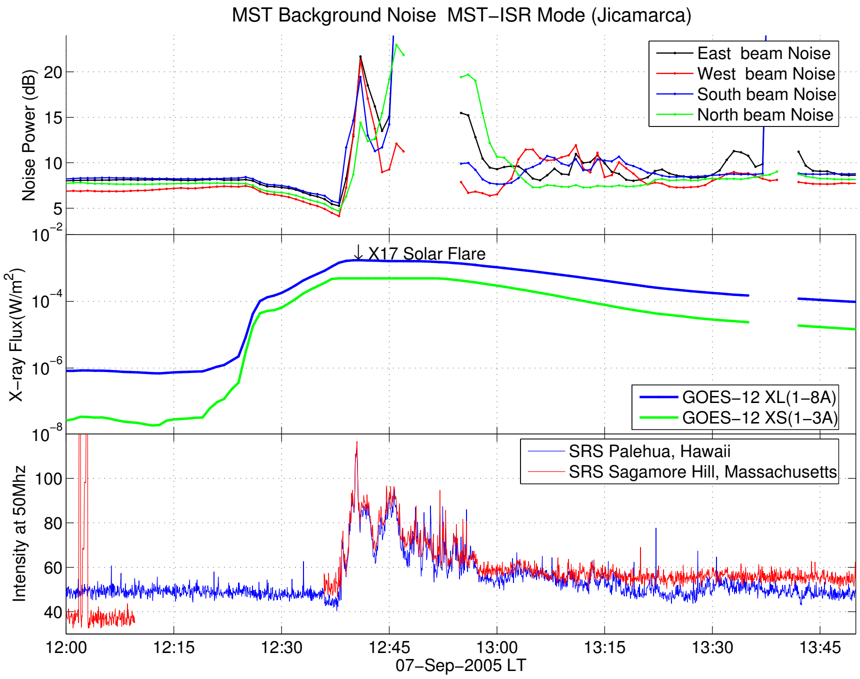

Figure 4.2 – The upper subplot shows the background sky-noise detected at JRO before and during the solar-flare event. The middle subplot shows the X-rays flux as obtained by the GOES-12 satellite and the lower plot shows the average signal intensity at 50 MHz ± 1 MHz detected by the observatories of Palehua in Hawaii and Sagamore Hill in Massachusetts.

The drop of about 3 dB in background noise level is well explained in terms of D-region absorption. This absorption, as explained in subsection 2.2.1, started to attenuate the background noise immediately after the enhanced X-ray flux penetrated Earth and started ionizing the lower part of the ionosphere. This phenomenon is known in the literature as sudden cosmic-noise absorption (SCNA) and is part of the sudden ionospheric disturbances (SID) explained in section 2.3.

The 50 MHz solar radio burst detected around 12:40 LT in the four JRO beams is corroborated by the observations done by the Palehua solar observatory in Hawaii, and the Sagamore Hill solar observatory in Massachusetts as shown in Figure 4.2. It should be mentioned that the main lobe of the antenna beam pattern was not directed towards the sun, meaning that the solar burst signal must have arrived from the sidelobes.

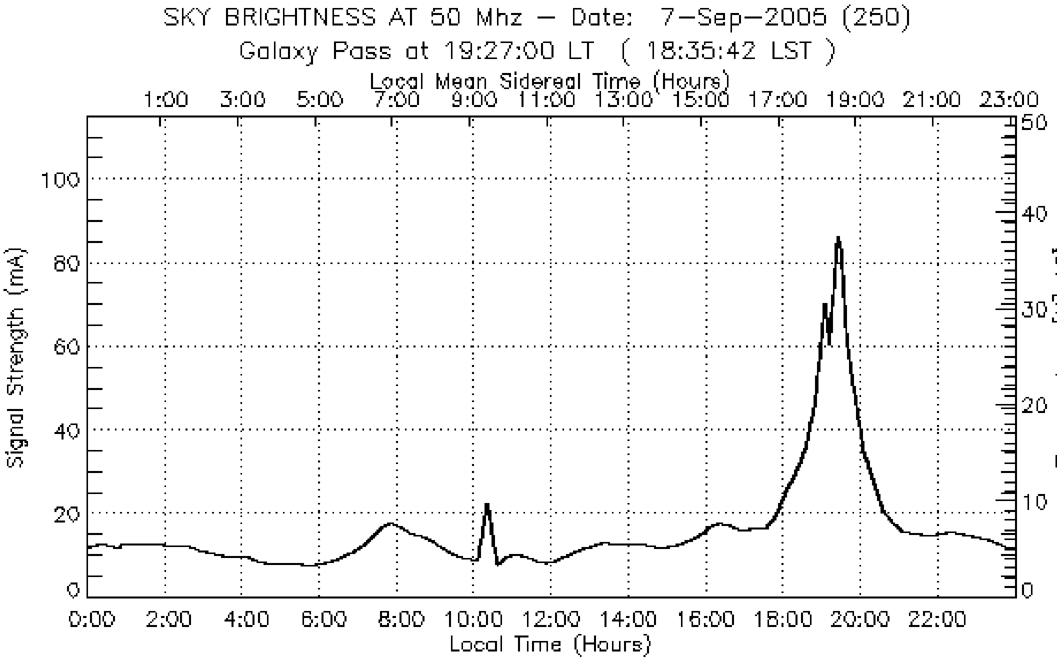

Figure 4.3 – Cosmic brightness at 50 MHz for September 07, 2005. This plot has been generated using the online tool found on the JRO website (`http://jro.igp.gob.pe/`).

Figure 4.3 shows the steady-state cosmic radiation as an antenna pointing on-axes at JRO would receive under normal conditions. In that figure the strong signal around 19:30 LT is the "galaxy pass" as it occurs when the antenna is pointing towards the center of our galaxy where a vast number of radio stars are located. Around 7:30 LT, another increase in cosmic radiation is attributed to the radiation coming from the opposite direction from the center of the Milky Way, usually called “back of the galaxy” where a vast number of other stars are also located. Finally, around 10:30 LT there is an increase of cosmic radiation coming from the “Hydra A” radio star in the Hydra constellation. The effect of the back of the galaxy and the Hydra pass can be seen in Figure 4.1 around 8:30 LT and 10:30 LT respectively rising the background cosmic radiation up to approximately 10 dB in the RTI map of normalized power.

The increase in noise detected at 50 MHz by JRO as well as in SRS observatories is related to the radio burst phenomenon on the sun as described by *Wild et al.* [1963]. Briefly, the burst is caused by the acceleration of plasma particles in the solar corona as described in subsection 2.1.2. It appears that the observed burst fits best what is described as type III with its associated type V radio emission as discussed in subsection 3.4.3.

4.1.2 Effects on the SNR of incoherent backscatter

Figure 4.4 shows the changes in the signal-to-noise ratio (SNR) of the ionospheric incoherent scatter returns detected in the four beams during the first 30 minutes of the solar flare event. The drop in SNR during the first 10 minutes following the onset of the flare can be explained by the increase in D-region absorption. In this case the effect of up to 3 dB of attenuation of the sky-noise detected at ground is doubled to 6 dB due to the fact that the radar signal is attenuated twice, once when propagation upwards, and in its way back to the radar. The SNR drops even further after the radio burst arrived to the antennas. This is of course a result of the burst signal causing effectively an enhanced background noise as far as incoherent scatter SNR calculations.

Due to the higher X-ray and UV solar radiation, the electron density experienced an enhancement at all ionospheric altitudes as will be seen later on an RTI map of electron density estimation from JRO data. This increase in electron density causes more Faraday rotation in the radar signal of the south beam, since it is the one pointing further away from perpendicular to $\vec{\mathrm{B}}$. The effect of higher Faraday rotation is to lower the “wiggle” as can be seen in the SNR map of the south beam in Figure 4.4. The “wiggle” before the flare centers around 400 km as seen from 12:00 to 12:25 LT. After the flare it can be seen that the center of the wiggle starts slowly to go lower in altitude down to approximately 350 km; this descent can be explained as an increase in Faraday rotation in the lower ionosphere. The wiggle also experienced a reduction in width, which can be attributed to an increase in electron density causing more Faraday rotation in the F-region. After the main phase of the flare, the center of the wiggle remained around 325 km and the width reduced to about 100 km, indicating an increased electron density in all ionospheric altitudes.

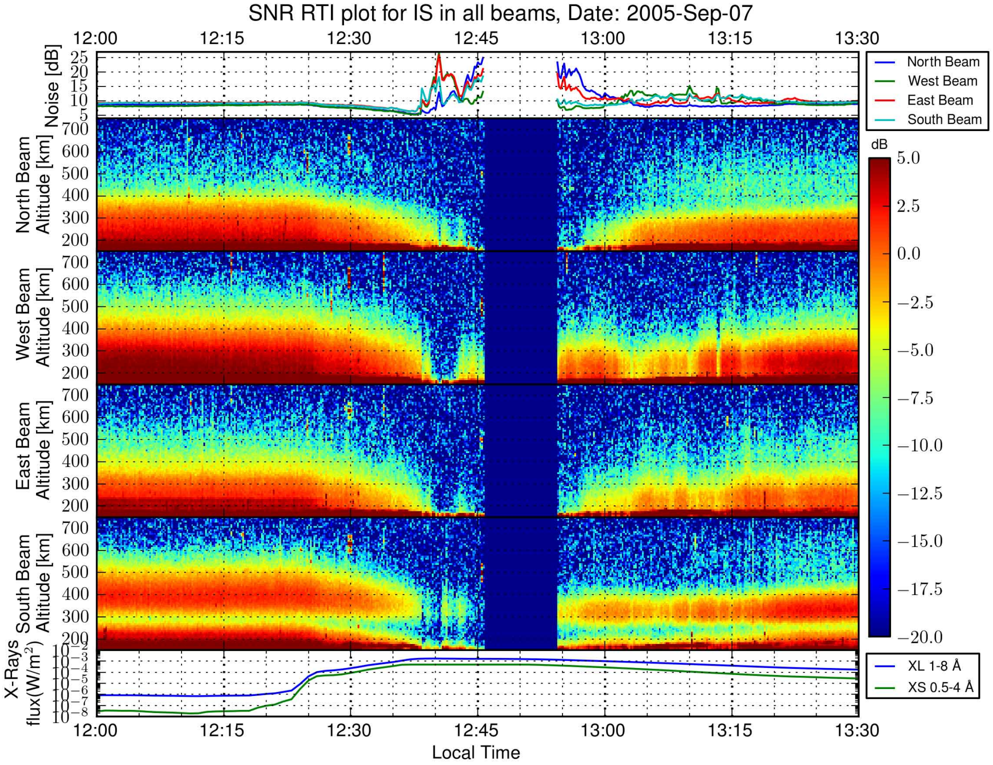

Figure 4.4 – SNR RTI plot of the IS parts of the four beams during the X17.1 solar flare on September 7, 2005. The plot in the top shows the cosmic noise power for each beam. The plot in the bottom shows the X-ray flux obtained from the GOES satellite.

4.1.3 Effects observed in the 150-km echoes region

The vertical Doppler velocities at the 150-km echoes region are shown in Figure 4.5. This vertical drift was calculated using spectral analysis, and it represents a probe for the vertical $\mathbf{E} \times \mathbf{B}$ drifts at F-region altitudes [*Kudeki and Fawcett*, 1993; *Chau and Woodman*, 2004]. Before the flare, the 150-km echoes Doppler velocities show a normal increasing behavior from 10 m/s at 9:00 a.m. LT up to 28 m/s at 11:30 a.m. LT, but at the time of the flare, the 150-km echoes mean vertical velocity drops dramatically down to 10 m/s as shown in the third subplot of Figure 4.5. The drop in velocity surely corresponds to a drop in the eastward electric field causing the $\mathbf{E} \times \mathbf{B}$ drifts. We do not know the specific mechanism in the disturbed ionosphere that may have caused such a drop. However, we do speculate that the field may have been reduced as a result of ionospheric electron density redistributions caused by the flare.

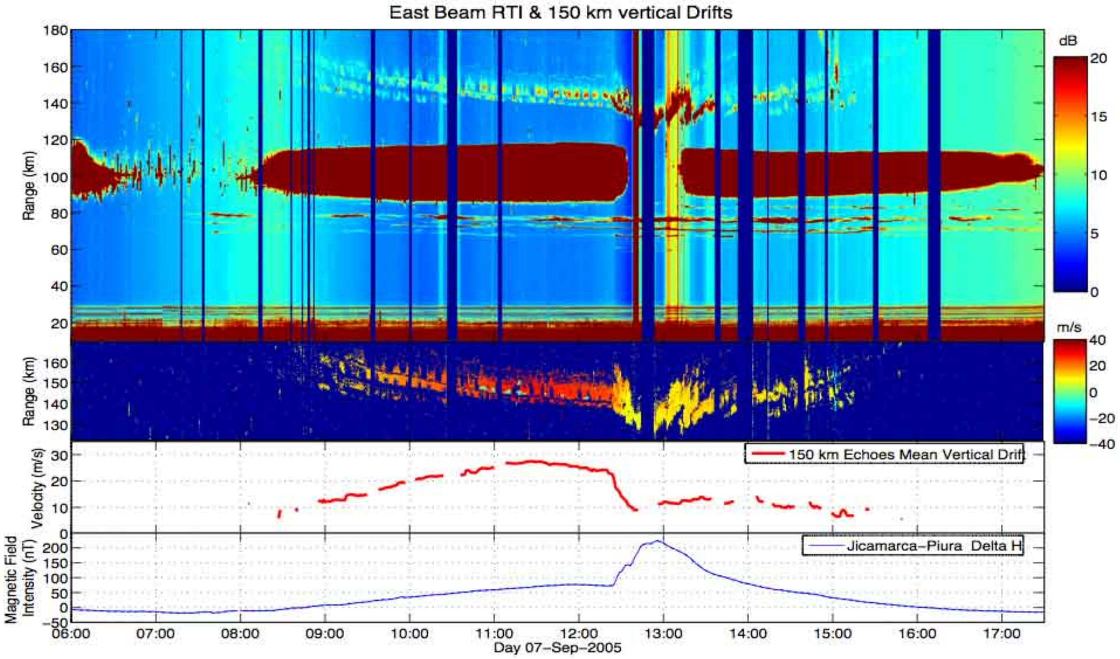

Figure 4.5 – RTI plot for the MST part of the east beam, 150-km echoes vertical drifts, and Jicamarca - Piura Delta H magnetometers data for September 07, 2005.

To observe how the shape and position of the 150-km echoes change during the solar flare, a high resolution, 12 seconds, integrated SNR map is presented in Figure 4.6 to capture the morphologic details of the 150-km echoes. At around 12:25 LT several layers of 150-km echoes seem to be squeezed together as if "pushed" by the solar radiation. The lower layer was pushed down for at least 10 km reaching its lowest level around 125 km of altitude, and the upper layers were pushed down about 20 km or even more, which remains unclear since layers that were not visible before the flare become visible during the main part of the flare. Finally it took about 2 hours for the 150-km echo signatures to recover from the disturbed state.

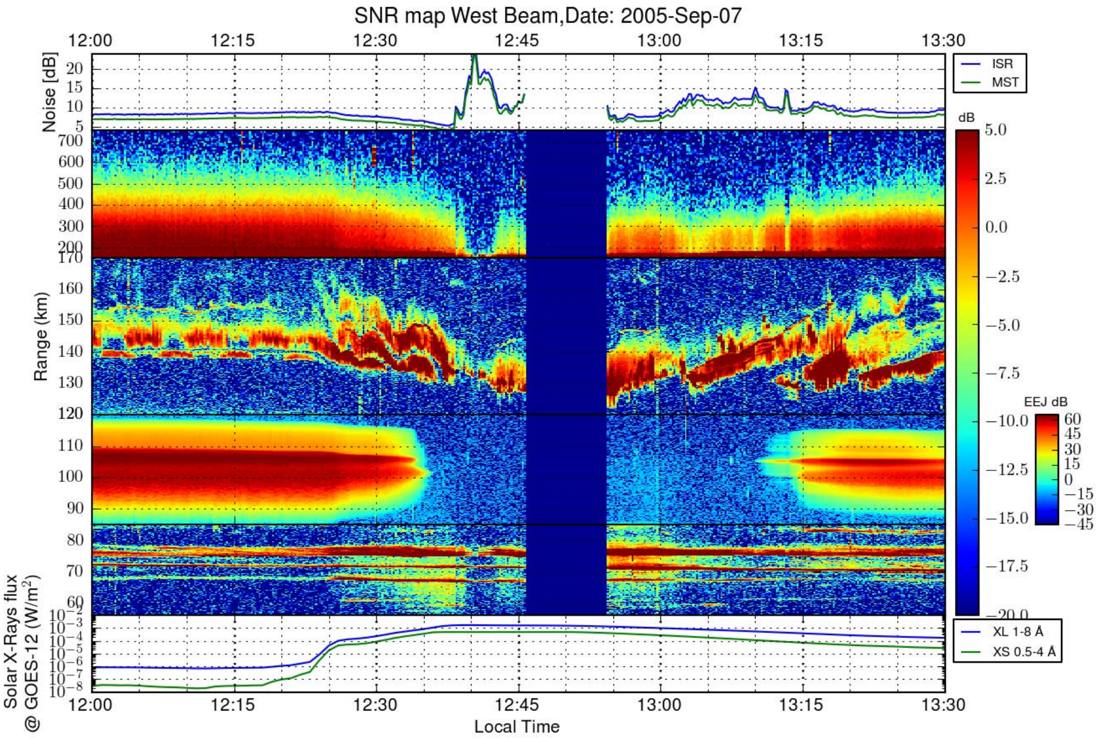

Figure 4.6 – Similar plot as Figure 4.1, in a 12 seconds time resolution, and in the region from noon to 13:30 hr LT. Notice how the layers of the 150-km echoes squeeze together as if "pushed" by the solar radiation. Layers that were not visible before the flare become visible. And it takes about 2 hours to recover from the disturbed state.

The drop in height of the 150-km echo layers does not correspond to a physical transport of existing pockets of irregular plasma since the vertical drift velocity remained upwards (although reduced) throughout the flare event. Instead, the observed drop must correspond to a change in the altitude of the background conditions driving the 150-km irregularities.

4.1.4 Response of the EEJ (equatorial electrojet) echoes to the solar flares

The equatorial E-region contains an intense zonal current known as the equatorial electrojet (EEJ) which exhibits a permanent state of microinstabilities and resultant density structures that scatter the 50 MHz radiowave echoes. The E-region is also characterized with a mean density profile with upward positive gradient during unperturbed daytime hours up to an altitude of $\sim$ 107 km (see *Farley* [2009]). In the disturbed ionosphere during a solar flare the density gradient is modified, which in turn has an effect on the distribution of radar echoes from the electrojet as shown in Figure 4.6 for the X17.1 solar flare. Right after the increase in X-ray flux around 12:25 LT, the EEJ backscatter power started to get weaker and thinner until disappearing around 12:35 L.T (10 minutes after the onset of the solar flare). The EEJ echoes were restored around 13:15 LT.

The high conductivity at the E-region and the confinement by the parallel geomagnetic field lines at the equator generate strong currents at the magnetic equator. Eastward current density $\vec{\mathbf{J}}$ and eastward electric field $\vec{\mathbf{E}}$ are related by

$$\vec{\mathbf{J}} = \sigma_c \vec{\mathbf{E}}, \tag{4.1}$$

where σ_c is known as Cowling conductivity (see *Farley* [2009]).

We can form an estimate of the variation of the electric field $\vec{\mathbf{E}}$, based on the mean vertical $\vec{\mathbf{E}} \times \vec{\mathbf{B}}$ drift of the 150-km echoes discussed in the previous subsection and the definition of the $\vec{\mathbf{E}} \times \vec{\mathbf{B}}$ drift velocity

$$\vec{\mathbf{v}} = \frac{\vec{\mathbf{E}} \times \vec{\mathbf{B}}}{\left|\vec{\mathbf{B}}\right|^2}, \tag{4.2}$$

which has a magnitude $\left|\vec{\mathbf{E}}\right| / \left|\vec{\mathbf{B}}\right|$. From the mean vertical drift velocity of the 150-km irregularities in Figure 4.5 we can estimate the velocity before and after the onset of the flare as $|\vec{\mathbf{v}}_1| \approx 25\,\mathrm{m/s}$ and $|\vec{\mathbf{v}}_2| \approx 10\,\mathrm{m/s}$ respectively. The magnetic flux density at the Earth's surface over JRO is approximately $\left|\vec{\mathbf{B}}\right| \approx 26000\,\mathrm{nT}$, and the daily variation, even under the flare conditions, is not that significant. It only varies by approximately $250\,\mathrm{nT}$ as shown in in Figure 3.5. Therefore we estimate the variation of $\left|\vec{\mathbf{E}}\right| = |\vec{\mathbf{v}}| \left|\vec{\mathbf{B}}\right|$ as $\left|\vec{\mathbf{E}}_2\right| / \left|\vec{\mathbf{E}}_1\right| \approx |\vec{\mathbf{v}}_2| / |\vec{\mathbf{v}}_1| = 0.4$. Using $\left|\vec{\mathbf{B}}\right| \approx 26000\,\mathrm{nT}$, the electric fields can be estimated to be $\left|\vec{\mathbf{E}}\right| \approx 0.65\,(\mathrm{mV})/\mathrm{m}$ and $\left|\vec{\mathbf{E}}\right| \approx 0.26\,(\mathrm{mV})/\mathrm{m}$ before and right after the onset of the flare respectively.

One way of detecting the effect of the current at the geomagnetic equator is to measure the difference in magnetic field intensity between a point at the magnetic equator (Jicamarca) and a point off the magnetic equator. A plot showing that Delta H difference is shown in Figure 4.5 between the stations of Jicamarca (geographic latitude of 11.95° south and a longitude of 76.87° west) and Piura (geographic latitude of 5.2° south and a longitude of 80.63333° west). We can do a rough estimate of the variation of the current as

$$\left|\vec{\mathbf{J}}_2\right| / \left|\vec{\mathbf{J}}_1\right| \approx \Delta \left|\vec{\mathbf{B}}\right|_2 / \Delta \left|\vec{\mathbf{B}}\right|_1 = 220\,\mathrm{nT}/70\,\mathrm{nT} = 3.14, \tag{4.3}$$

where the magnitude of the magnetic flux densities has been calculated using the three components of the Jicamarca-Piura ΔH shown in Figure 3.7. Based on this magnetic field difference we can affirm that the EEJ current was increased by a factor of 3 during the solar flare. Furthermore, from the current density equation in (4.1) , and taking the variation of the electric field and the variation of the current density at the geomagnetic equator, we can estimate that the E-region conductivity increased as a factor of

$$\sigma_2/\sigma_1 \approx \frac{\left|\vec{\mathbf{J}}_2\right| / \left|\vec{\mathbf{J}}_1\right|}{\left|\vec{\mathbf{E}}_2\right| / \left|\vec{\mathbf{E}}_1\right|} = \frac{3.14}{0.4} = 7.85, \tag{4.4}$$

which at the same time assumes an increase in electron density by a similar factor.

Finally, we conclude that the E-region current increased, but due to the redistribution of the concentration of electrons, the density profile must no longer have a positive gradient. As a consequence, the conditions for the existence of EEJ echoes disappear and the echoes were suppressed as shown in Figure 4.6.

4.1.5 Enhancement of the mesospheric echoes

As seen in Figure 4.6, the SNR of mesospheric returns increases initially after the onset of the solar flare. This is consistent with earlier studies of D-region response to X-rays solar flares [e.g. *Rastogi et al.*, 1988]. They showed such an increase and explained it using the gradient-mixing hypothesis. Another explanation of the increase in SNR is the fact that the background cosmic noise at 50 MHz has been reduced, and at least for the lower part of the D-region, that reduction will contribute to the detectability of the mesospheric echoes. But it can be seen that right after the onset of the solar flare, the mesospheric SNR increased significantly (roughly from 0 to 5 dB) while the attenuation of the cosmic noise in the D-region was about 1 dB. The increase in mesospheric returns can also be seen from the RTI map in Figure 4.1 since it has not been normalized by the background noise.

4.1.6 Mesospheric RCS changes during the flare

As described in section 3.5.2, the MST-ISR experiments were designed for absolute RCS observations. Using the technique described in *Lehmacher et al.* [2009] and *Akgiray* [2007], both ionospheric electron density measurements and mesospheric RCS estimates were obtained.

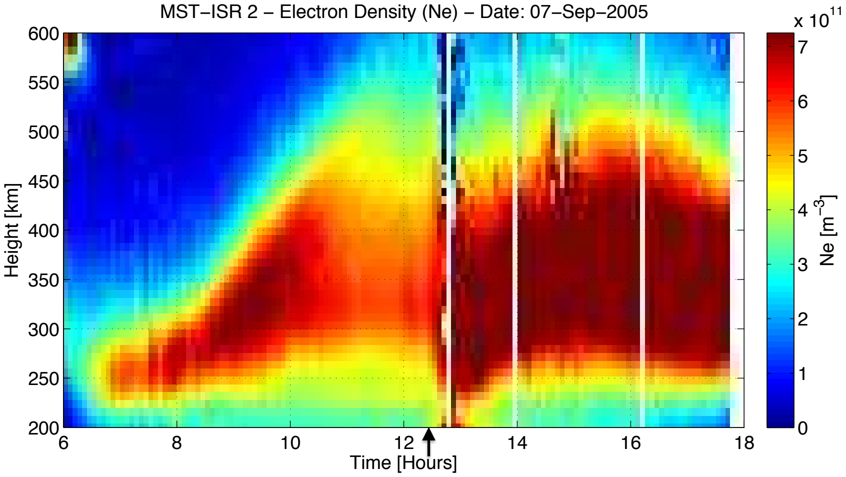

Figure 4.7 – Plot showing a map of electron density (N_e). The arrow around 12:30 LT indicates the onset of the solar flare. (Presented at 2009 CEDAR Workshop, *Reyes et al.* [2009].)

In Figure 4.7 the electron density N_e map is shown as a result of applying IS techniques to invert for electron density N_e based on the information from the four radar beams and the magneto-ionic theory. The result from the inversion technique showed that the electron density increased during the solar flare at all altitudes as discussed in section 4.1.2. The lower part of the ionosphere experienced a larger increase in N_e than higher up. For instance, around 200 km, N_e increased from roughly 3.5×10^{11} m^{-3} before the onset of the flare to 6.5×10^{11} m^{-3} a quarter of hour later, while at 350 km the increase was only from about 5.5×10^{11} m^{-3} to 6.5×10^{11} m^{-3}.

The compensation due to the D-region absorption is reflected in the variation of the calibration parameters shown in Figure 4.8. Those calibrating parameters, as explained in section 3.5.2, are parameters multiplying the transmitted power in the soft-target radar equation. Therefore any variation in the transmitted power as well as losses in the propagation path will be reflected in their value. As shown in Figure 4.8 the calibration parameters start dropping until reaching a maximum drop of $1.5/0.2 \approx 7.5$ from the onset of the solar flare. Assuming that around 12:30 LT, the only losses that changed were those due to D-region absorption, then the total 2-way D-region attenuation reached a maximum of $10\ \log_{10}(7.5) = 8.75\,\mathrm{dB}$ (i.e. a total 1-way attenuation of 4.37 dB). To compare this value with the $-3\,\mathrm{dB}$ attenuation of the cosmic background noise shown in Figure 4.2, we need to use the calibration parameters values for the time right before the solar radio burst, i.e around 12:35 LT. In Figure 4.8 each point represents an integration of 5 minutes. The drop from the onset of the flare until right before the radio burst hit Earth is $1.6/0.4 \approx 4$. This corresponds to a 1-way total D-region attenuation of $10\ \log_{10}(4/2) = 3\,\mathrm{dB}$ which is in agreement with the cosmic background attenuation detected at that time.

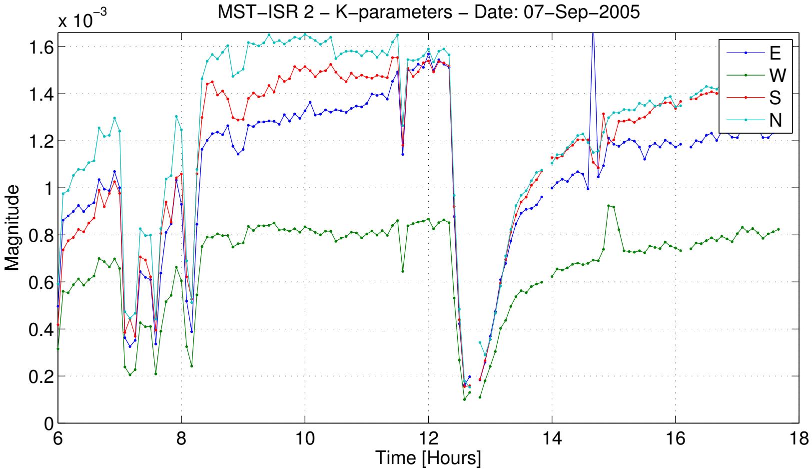

Figure 4.8 – Plot showing the calibration parameters for each acquisition channel. Note that when the flare happens, the calibration parameters compensate for the D-region absorption. In general these parameters reflect the loss in power due to any factor. (Presented at 2009 CEDAR Workshop, *Reyes et al.* [2009].)

The drops around 7:00 LT were due to failures in the transmitter that the technique is trying to compensate for. These parameters were applied to the MST region to obtain absolute RCS for the mesospheric and 150-km region echoes as shown in Figures 4.9 and

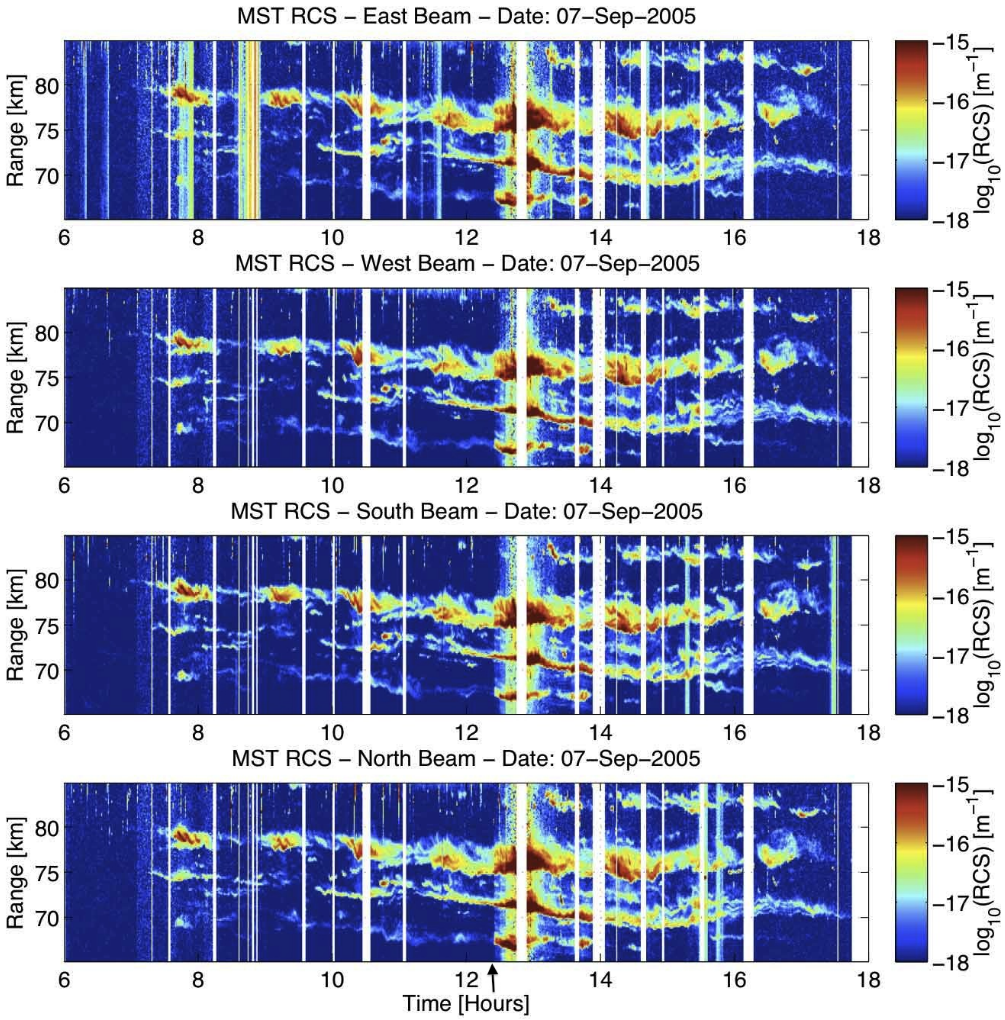

Figure 4.9 – Plot showing the absolute RCS of mesospheric echoes. (Presented at 2009 CEDAR Workshop, *Reyes et al.* [2009].)

4.10 respectively.

Notice that the calibration parameters used in this technique were obtained using the IS backscatter from the F-region, and they reflect the total accumulation of D-region absorption. In that sense, when the circumstances are such that the D-region absorptions is important (e.g. during solar X-ray flares), the calibration parameters to get absolute RCS should be applied only for MST region altitudes that are above the absorption regime (e.g. EEJ or 150-km echoes). To obtain the correct RCS for the D-region we should consider altitude dependent calibration parameters, since the losses for the lower part of the mesosphere will be less than for the upper part. Doing the correct estimation of RCS during the presence of D-region absorption will remain as future work. One way around that difficulty is using the electron density estimates given by the ionosonde, the neutral density, and a model for the collision coefficients to estimate the absorption that 50 MHz signals will suffer at every altitude, and scale down the overestimated RCS of the lower part of the mesospheric returns. In Chapter 5 a discussion about altitude dependent calibration parameters will be given.

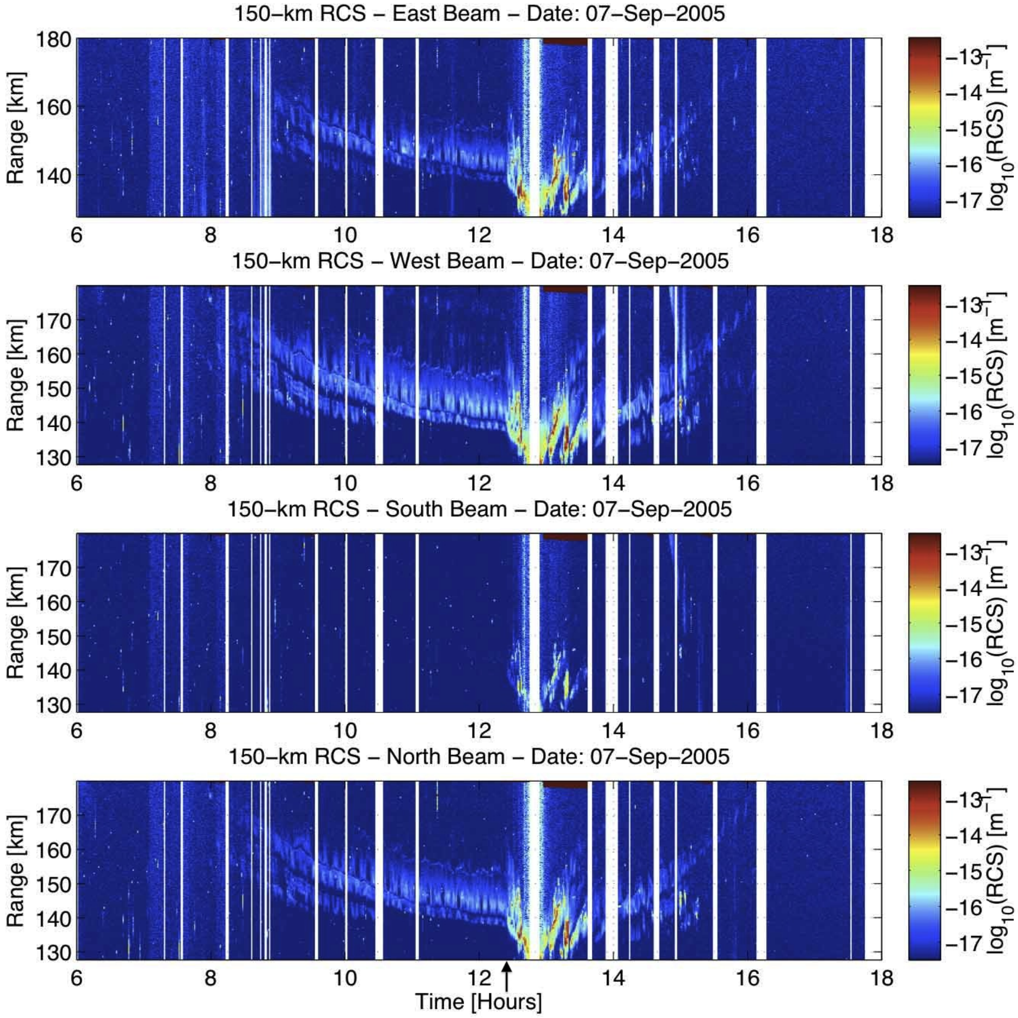

Figure 4.10 – Plot showing the absolute RCS of 150-km echoes for the four beams of MST-ISR. (Presented at 2009 CEDAR Workshop, *Reyes et al.* [2009].)

4.2 X5.5 Solar Flare on Sept. 08, 2005

Figure 4.11 shows RTI maps of the normalized radar returns at JRO on September 08, 2005. On this day, the effects caused by solar flares of different X-ray flux intensities can be explored. From the X-ray flux plot shown in Figure 3.2 we can identify up to three important X-ray flares in the period of time pertinent to our JRO data, the X5.5 around 16:00 LT, and two M2.1 flares, one around 12:00 LT and the other one around 15:30 LT.

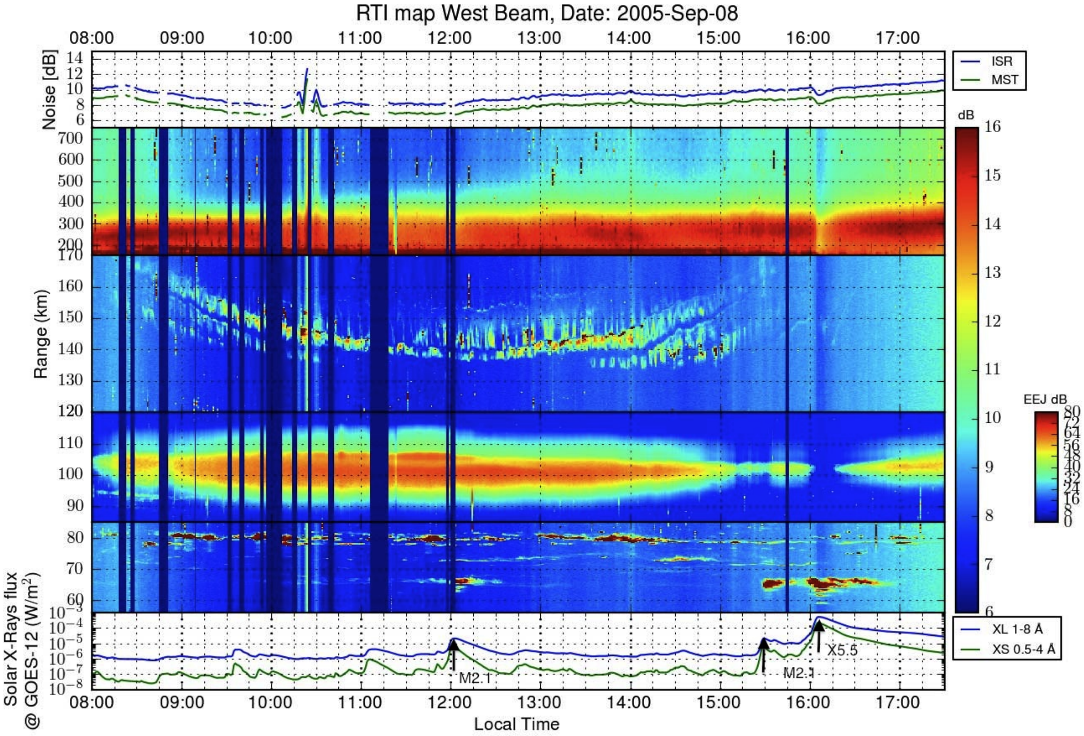

Figure 4.11 – RTI map for the west beam together with solar X-ray flux from GOES satellite. The X5.5 solar flare around 16:05 LT influenced an increase in D-region backscattering around 65 km, and affected the location of the 150-km echoes, suppressed the EEJ and increased the D-region absorption. Two more flares caused an impact to the data this day: an M2.1 solar flare at noon and an M2.1 around 15:30 LT. These lower intensity flares only had an influence on the D-region, enhancing the mesospheric echoes around 65 km.

The effect of the M-class solar-flares is evident only in the lower part of the mesospheric echoes as shown in Figure 4.11. The M2.1 solar flares produced an enhancement of the backscatter signal around 65 km at noon and at 15:30 LT. The X-class solar flare caused also an increase in backscatter signal from the lower part of the D-region. It also suppressed the echoes from the EEJ and attenuated the background cosmic noise as well as the IS backscatter signal. Finally, the 150-km echoes were pushed down about 10 km as in the previous analyzed day.

The background cosmic noise under non-disturbed circumstances does not have a significant day to day variability, so it will look similar to the one shown in Figure 4.3. In Figure 4.11 we can notice the back of the galaxy passing around 8:00 LT and Hydra passing around 10:30 LT as expected by the non-disturbed background noise. The anomalous attenuation of the cosmic background noise by about 1 dB right after the X5.5 solar flare at 16:00 LT can be explained by the increase in D-region absorption following the X5.5 solar flare.

As shown in the SRS plots in Figures 3.17 and 3.18, a weak solar radio burst hit Earth around 16:11 LT. Nevertheless its radiation energy was not enough to be detectable by the sidelobes of the JRO antenna beam patterns as in the case of September 07, 2005.

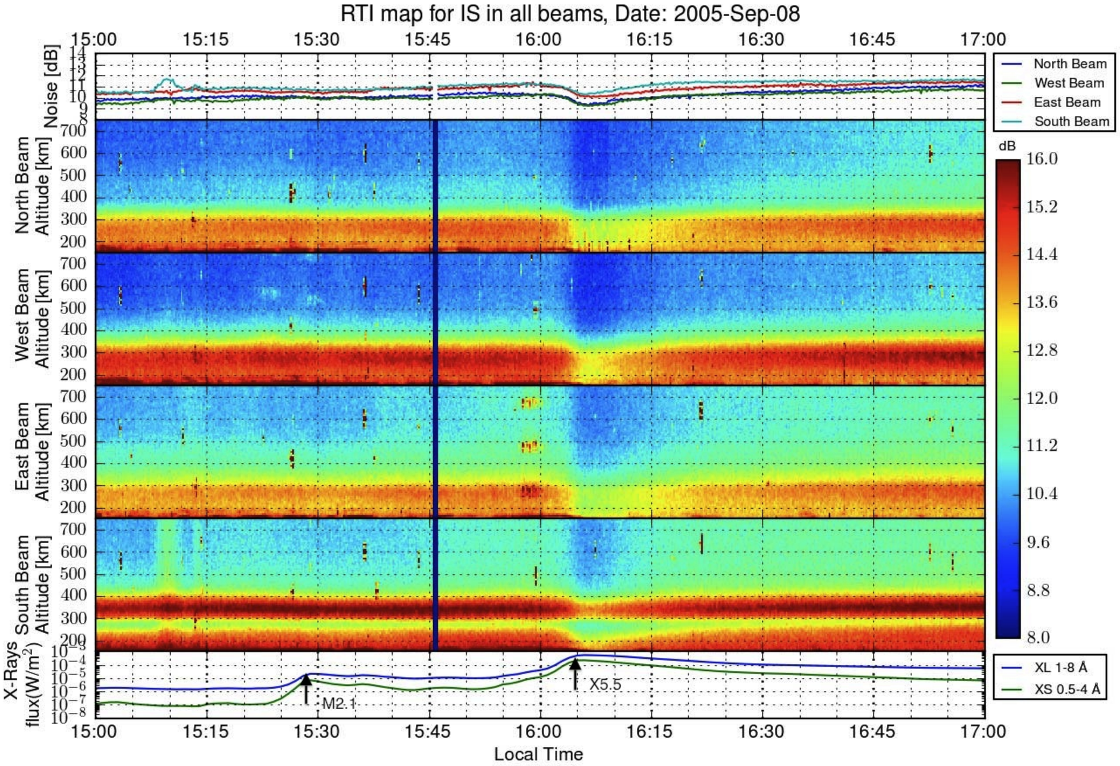

Figure 4.12 – RTI map of the IS parts of the four beams during the X5.5 solar flare on September 08, 2005. The plot in the top shows the cosmic noise power for each beam. The plot in the bottom shows the X-ray flux obtained from the GOES satellite.

Figure 4.12 shows the changes in the RTI of the IS returns in the four beams from 15:00 to 17:00 LT on September 08, 2005. The drop by about 2 dB in IS power due to D-region atmospheric absorption is in agreement with the 1 dB drop in background cosmic noise and last for about 5 minutes. With no other apparent source of ionization, 10 minutes after the flare, the F-region returned to its status before the flare. This can be seen from the altitude and width of the "wiggles" in the south beam before and after the X5.5 flare. Although, right after the onset of the X-type solar flare, there was an increase in Faraday rotation in the lower part of the ionosphere, which indicates some enhancement of the D-region electron density.

From the EEJ RTI map in Figure 4.11, right after the X5.5 solar flare around 16:05 LT the EEJ backscatter power disappeared for about 15 minutes. This can be explained similar to the previous case on September 07. The redistribution of the electron density profile at the lower ionosphere has as a consequence the suppressing of echoes from the EEJ region. The E-region currents on the contrary experienced an intensification, detected by the increase of magnetic flux density at the geomagnetic equator. This can be seen in the magnetometer data from Huancayo, Peru, around 21 universal time (UT) (16 LT at JRO) as shown in Figure 3.8. As discussed in section 3.2, this increase in magnetic flux density, named "magnetic crochet", is the consequence of stronger electric currents due to enhanced electron density in the E layer of the ionosphere.

From the RTI map showing mesospheric returns in Figure 4.11 we can see that M2.1 solar flares at 12:00 LT and at 15:30 LT had an influence in the increase in backscattering power from the lower part of the D-region around 65 km. Upper layers of the mesosphere remain unaltered after the M2.1 solar flare radiation hit Earth. When the X-ray radiation of the the X5.5 solar flare arrived to Earth, the lower part of the mesosphere also increased its backscattered power, and due to D-region absorption, the upper layers got attenuated.

4.3 X6.6 Solar Flare on Dec. 06, 2006

Similar to the cases studied in the two previous sections (Sept. 7 and 8, 2005), the main features of the solar flare effects for December 06, 2006, are shown in SNR maps in

Figure 4.13. On this day, the effects of two major solar flares will be analyzed. First a solar flare with classification X6.6 around 13:45 LT, and then one classified as M3.5 around 15:15 LT. See Figure 3.3 to see how the X-ray flux detected at GEOS-12 varied throughout the day with their corresponding classified solar flares.

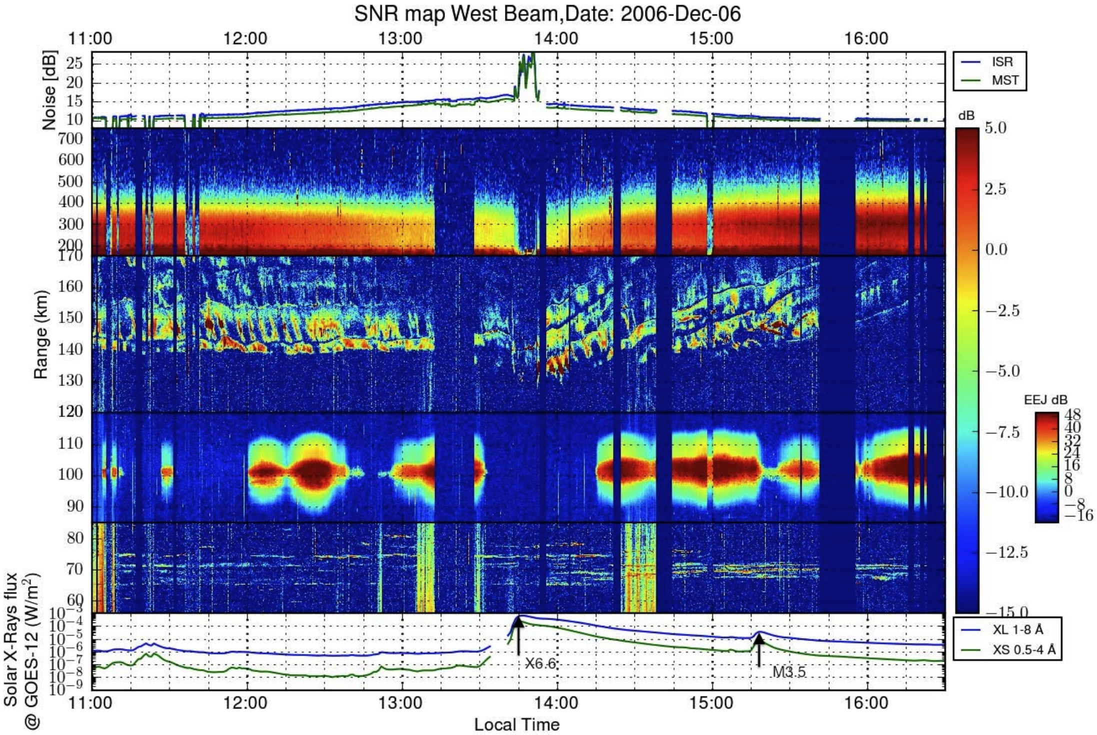

Figure 4.13 – SNR map and solar X-ray flux from GOES satellite for December 06, 2006. The X6.6 solar flare around 13:45 LT caused an increase in electron density in the F-region; D-region layers in the range from 65 km to 70 km where enhanced; the 150-km echoes were "pushed" down by about 15 km and the already pulsating EEJ echoes remained suppressed. Next, the M3.5 solar flare around 15:15 LT had an impact in the 150-km echoes and reduced the EEJ echoes for about 10 min.

From Figure 4.14 we notice that the electron density increased in all ionospheric regions. This can be seen from the "wiggles" in the south and north beams. In the south beam the main wiggle was centered around 350 km before the X6.6 solar flare, and went down to 325 km. Another wiggle appeared centered around 425 km in the south beam, at the same time that a wiggle start been detected around 400 km in the north beam. All this is indication of increased Faraday rotation due to in increase in electron density at all ionospheric regions. The M3.5 flare did not have much of an impact in the IS electron

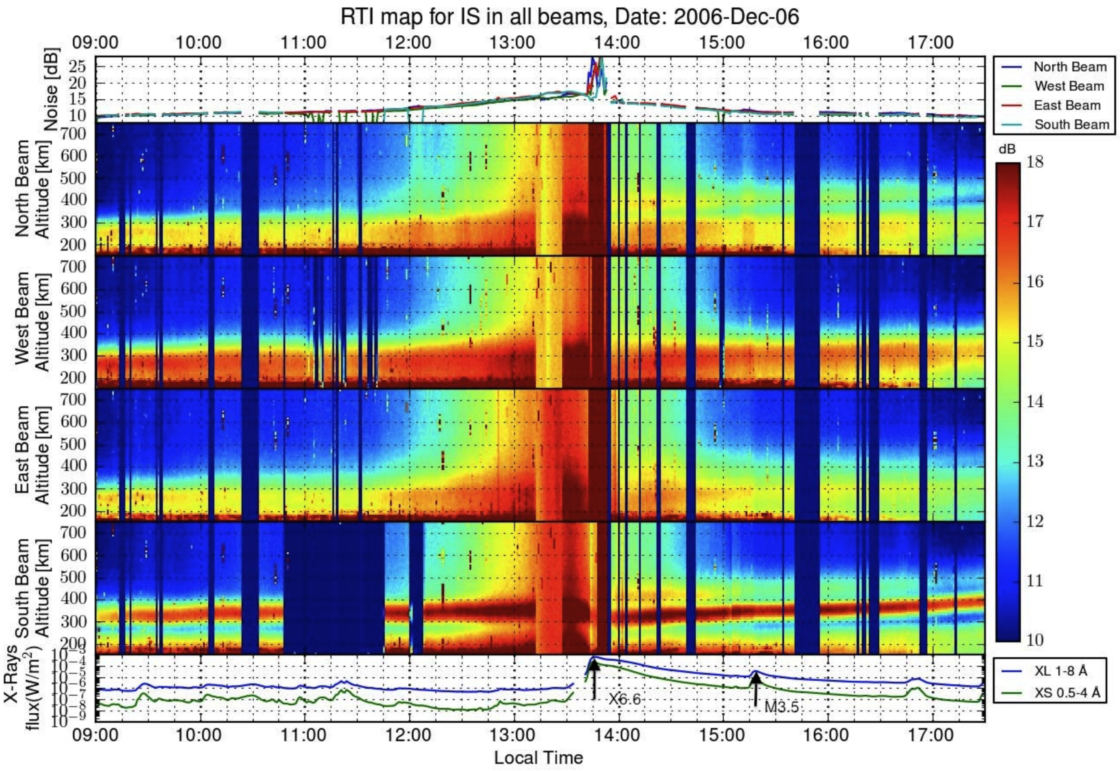

Figure 4.14 – RTI map of the IS parts of the four beams during the X6.6 and the M3.5 solar flares on December 06, 2006. The plot in the top shows the cosmic noise power obtained by each beam. The plot in the bottom shows the X-ray flux obtained from the GOES-12 satellite.

density.

The cosmic background noise detected by the south beam experienced a couple of decibels of attenuation around 13:45 LT as shown in Figure 4.14 . This can be explained by the increase in D-region absorption. The X6.6 solar flare increased the electron density at the D-region, resulting in the increase in D-region absorption for 50 MHz signals. This attenuation is not noticeable in the other beams since the solar radio burst was detected on those beams almost at the same time of peak in X-ray flux. The solar radio burst increased the cosmic background noise in all the beams by about 10 dB to 15 dB. This solar burst, like that on Sept. 07, 2005, appears to fit best what is described as type III with its associated type V radio emission (see section 3.4.3).

The overall increase in cosmic background noise with a power peak of 17 dB around 13:30 LT is the pass of the galaxy. This is in agreement with the expected cosmic brightness

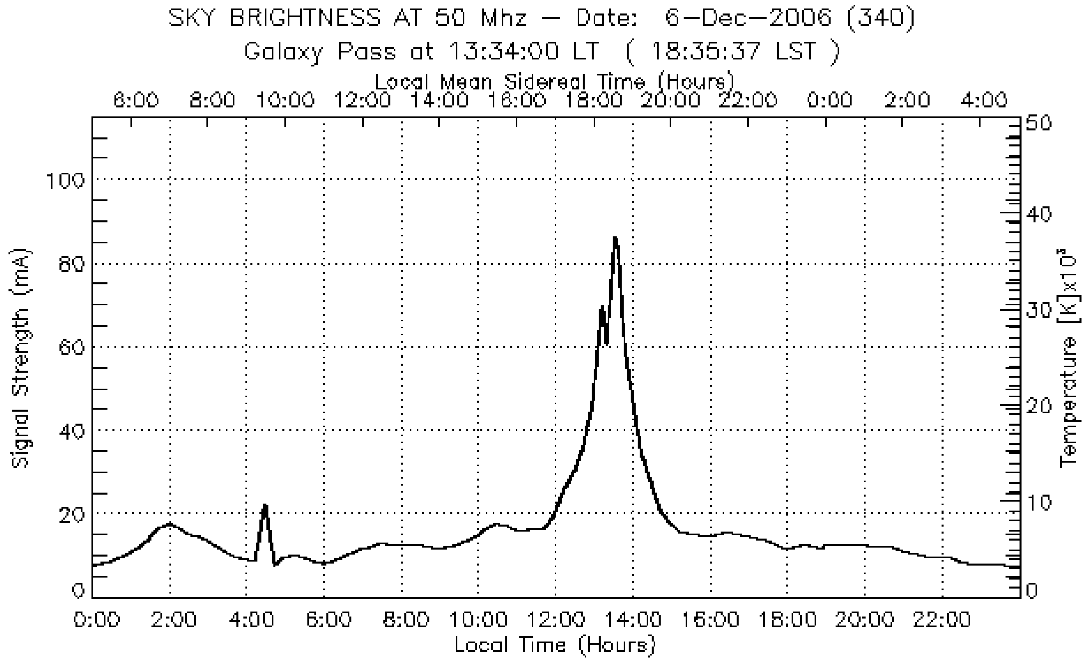

Figure 4.15 – Cosmic brightness at 50 MHz for December 06, 2006. This plot has been generated using the online tool found on the JRO website (`http://jro.igp.gob.pe/`).

at 50 MHz shown in Figure 4.15.

Both the X6.6 and the M3.5 solar flares had an impact on the 150-km echoes as can be seen in the SNR map of Figure 4.13. The X6.6 flare lowered the 150-km layers by about 10 km and increased the backscattered power of the lower layer. The M3.5 flare lowered the 150-km echoes, but only a few kilometers, and it also increased the backscattered power of the lower layer of the irregularities.

The already pulsating EEJ echoes remained suppressed during the main phase of the X6.6 flare. For the case of the M3.5 flare, the EEJ returns got strongly attenuated during approximately 10 min.

D-region layers in the range from 65 km to 70 km where enhanced by the X6.6 flare. No detectable changes were found in the D-region layers during the M3.5 flare

CHAPTER 5

CONCLUSIONS AND FUTURE WORK

The effects of six X-ray flares of different intensities on MST-ISR data have been analyzed in Chapter 4 and their main effects on the ionospheric radar backscatter signals are listed in Table 5.1 at the end of this chapter. The main conclusions drawn from the studies described on this thesis can be summarized as follows:

1. D-region backscatter power increased in all the solar flares analyzed. Mesospheric lower layers that were not detected before the flare become visible. Table 5.1 indicates the lowest detected layers.

2. Effects of D-region absorption at 50 MHz caused by the increased electron density at mesospheric altitudes are detectable for solar flares with intensities of at least M3.5. As shown in Table 5.1 the total D-region attenuation increases as the X-ray flux increases. The attenuation has been observed in the drop in the cosmic radiation power, and in the IS backscatter power. In the latter, the attenuation is doubled because the signal is attenuated on the way up an on the way down. The total attenuation in the D-region has also been detected in the calibration constants K_i, that compensate for any losses in the propagation path.

3. Effects on the 150-km irregularities start to become detectable for solar flares with intensities of at least M3.5. Layers seem to be squeezed together as if "pushed" by the solar radiation. The layers are also pushed down several kilometers depending on the intensity of the X-ray flux. Layers that were not visible become visible during the main phase of the flare. The location of the echoes were restored after a couple

of hours in the case of the X17.1 and after approximately one hour in the case of the X6.6 flares. Therefore the recovery time of the location of the 150-km irregularities depends on the intensity of the flare. The $\mathbf{E} \times \mathbf{B}$ drift obtained from the 150-km echoes are not related with the drop in location of the physical transport of the existing 150-km structures. The drift shows a drop during the flare and remains low during the whole recovery time. This drop indicates a decrease of the eastward electric field $\mathbf{E}$ which might have been due to the rearrangement of electron density in the ionosphere caused by the flare.

4. Equatorial E-region current increases during solar flares with intensities of at least M3.5. This increase is detected by the increase of the difference in magnetic field intensity between JRO and Piura (located 800 km to the north of Lima). Even though the electric field decreases, the increase in electron density causes the Cowling conductivity to increase further more to allow for an enhanced current. On the contrary, the EEJ echoes were suppressed because the electron density profile might no longer exhibit an upward gradient at the E-region as needed for scattering the 50 MHz radiowaves during the daytime [e.g. *Farley*, 2009].

The calibration constants K_i obtained using the technique described in subsection 3.5.2 were calculated using the F-region IS. Therefore they account for the total 2-way attenuation through the D-region. The obtained mesospheric RCS shown in Chapter 4 were obtained using those calibration constants and need to be adjusted using altitude dependent calibration constants $K_i(h)$. The altitude dependent $K_i(h)$ is needed since the compensation due to D-region absorption is proportional to the 2-way attenuation. This attenuation depends on the electron density and varies with height as shown in section 3.5.3.

Different electron density profiles with the same total 2-way attenuation can have different profiles of altitude dependent calibration parameters $K_i(h)$ in the D-region. At 50 MHz, the altitude dependent attenuation in the D-region depends almost solely on the electron density profile as described in section 2.2.1. Therefore an estimate of the D-region electron density is needed to adjust the RCS of the mesospheric returns. The estimation of these new altitude dependent calibration constants will remain part of a future work, and will allow us to better estimate the RCS of mesospheric echoes during solar flare events.

Table 5.1 – Summary of the effects caused by solar flares of different intensities in the MST-ISR data.

Solar flare type	Time of occurrence	Maximum 1-way D-region attenuation	D-region backscatter power	150-km irregularities	EEJ	IS backscatter power	50 MHz solar radio burst
M2.1	12:00 and 15:30 LT on Sep. 08, 2005	-	Enhanced SNR. Layers detected from 65 km.	-	-	-	-
M3.5	15:15 LT on Dec. 06, 2006	< 1 dB	Enhanced SNR. Layers detected from 65 km.	Echoes pushed down by about 1 km. Stronger SNR in lower layer.	Echoes strongly attenuated for 10 min.	Attenuated by < 1 dB.	-
X5.5	16:00 LT on Sep. 08, 2005	≈ 1 dB	Enhanced SNR. Layers detected from 60 km.	Echoes pushed down by about 10 km. Only lower layer visible at 16 LT.	Echoes disappeared for 15 min.	Attenuated by 2 dB.	-
X6.6	13:45 LT on Dec. 06, 2006	≈ 2 dB	Enhanced SNR. Layers detected from 65 km.	Echoes pushed down by about 15 km. Stronger SNR in lower layer.	Echoes not present.	First attenuated by 4 dB. Then N_e increased compared with pre-flare conditions.	Type III and V
X17.1	12:30 LT on Sep. 07, 2005	≈ 4.4 dB	Enhanced SNR. Layers detected from 60 km.	Echoes pushed down by about 20 km. Stronger SNR in all layers. $\mathbf{E} \times \mathbf{B}$ drift drop by 18 m/s.	Echoes disappeared for 45 min.	First attenuated by 8 dB. Then N_e increased compared with pre-flare conditions.	Type III and V

APPENDIX A

SOLAR RADIO SPECTROGRAPHS (SRS) DATA STRUCTURE

The data for the SRS plots shown section 3.4 is stored in SRS data files from the solar observatories and can be obtained from the NOAA National Geophysical Data Center (NGDC) ftp site `ftp://ftp.ngdc.noaa.gov/STP/SOLAR_DATA/SOLAR_RADIO/SPECTRAL_RSTN`. The files used have the filenames “SSyymmdd.srs”, where SS represent the observatory abbreviation (see Table 3.2). The filename also contains the local date specifying the last two digits of the year “yy”, then the number of the month “mm” (01 to 12) and the day of the month “dd” (01 to 31).

Table A.1 – Format of the data record in the SRS files. Heather structure and data.

Byte#	Description	Format
1	Year (last 2 digits)	Byte integer (unsigned)
2	Month number (1 to 12)	Byte integer (unsigned)
3	Day (1 to 31)	Byte integer (unsigned)
4	Hour (0 to 23 UT)	Byte integer (unsigned)
5	Minute (0 to 59)	Byte integer (unsigned)
6	Second at start of scan (0 to 59)	Byte integer (unsigned)
7	Site Number (0 to 255) see table 3.2	Byte integer (unsigned)
8	Number of bands in the record (2)	Byte integer (unsigned)
9,10	Band A - Start Frequency (MHz)	Word integer (16 bits)
11,12	Band A - End Frequency (MHz)	Word integer (16 bits)
13,14	Band A - Number of bytes in data record (401)	Word integer (16 bits)
15	Band A - Analyzer reference level	Byte integer (unsigned)
16	Band A - Analyzer attenuation (dB)	Byte integer (unsigned)
17-24	Band B - Similar than bytes 9 - 16 from Band A	
25-425	401 data bytes for band 1 (A - Band)	
426-826	401 data bytes for band 2 (B - Band)	

The files consist of several binary records, each of length 826 bytes corresponding to a single sweep of frequencies from 25 MHz to 180 MHz in two bands: 25 - 75 MHz (Band A) and 75 to 180 MHz (Band B). The data record consists of a 24 byte header record followed by two arrays of 401 data bytes each as depicted in the table A.1. The 401 data bytes correspond to the following frequencies

$$f = \text{start freq.} + (\text{end freq. - start freq.}) \times (n - 1)/400\,\text{MHz}, \tag{A.1}$$

where "start freq." and "end freq." are the start and end frequencies in MHz specified in the data header (see Table A.1) and n is the n-th data byte.

APPENDIX B

THE RADAR ACQUISITION SYSTEM

The receiver circuit is shown in Figure B.1. It starts by collecting signal from the antenna pairs after the spark gaps Transmit/Receiver (T/R) switches. After the lines reach the receivers room, the signal passes through a new set of diode limiters that offer more bandwidth than the older cavity limiters. The signal is then amplified using tuned amplifiers (Frond ends) that boost the signal by 24 dB each, and is calibrated with a set of attenuators to obtain similar signal levels in the four channels. This RF amplifiers (model P50VDG) made by "ARR communications Products" have $50\,\Omega$ impedance at the input and output and have a 24 dB gain with a bandwidth of 4 MHz and 0.5 dB of noise figure. Before the signal is fed into the receivers it is passed through a set of voltage limiters to protect the digital receivers from signals larger than 1Volt peak to peak.

The digital receivers are two Echotek 210 (ECDR-GC-214-PCI) cards placed inside a PC working simultaneously, each acquiring the signals of two antennas making a total of 4 receiver channels. These receivers use a 60 MHz external clock that is obtained from a stable common oscillator of 10 MHz that is upshifted using a x6 frequency multiplier as shown in the left bottom part of Figure B.1. The same 60 MHz clock is used for the digital receivers, the radar controller and the Direct Digital Synthesizer (DDS) to guarantee the coherence between the receiver and transmitter frequencies. When a 10 MHz GPS disciplined oscillator is used, the system is capable of performing bi-static experiments.

The ECDR-GC214-PCI card contains the receiver chip GC4016, which encloses three important steps of filtering for each of their four receiving channels available as shown in Figure B.2. The first step is a five-stage Cascade Integrate Comb (CIC) filter, followed by

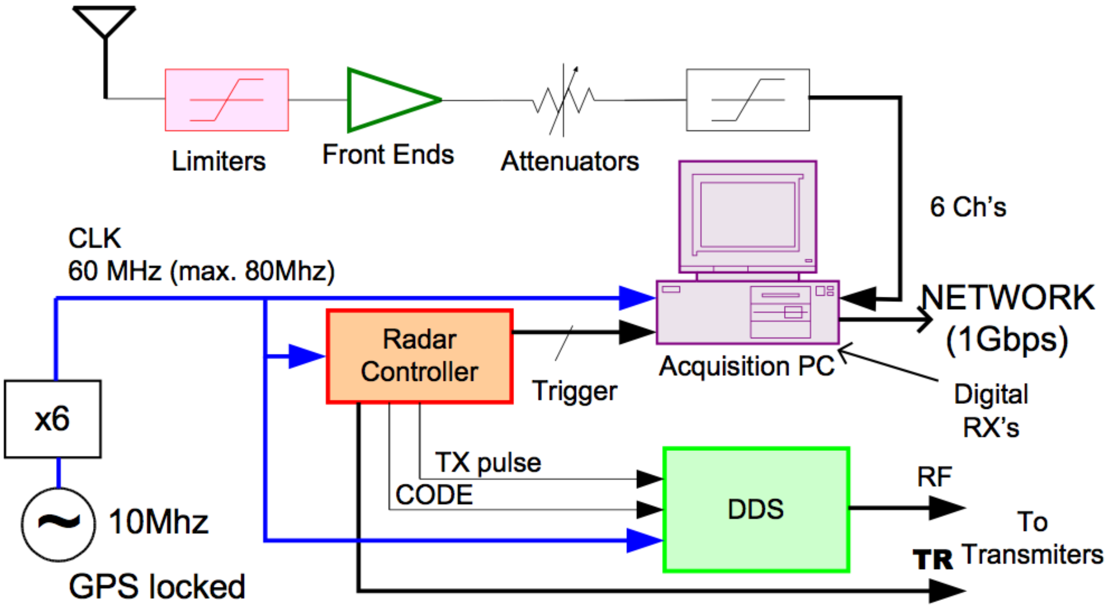

Figure B.1 – Digital receivers based Jicamarca acquisition system used in the MST-ISR campaigns.

a decimate-by-two compensated finite impulse response (CFIR). The CFIR compensates the droop in the CIC filter passband as shown in Figures B.3 and B.4. The matched filter is performed with the last programmable and decimate by two FIR filter. The calculated frequency response of all the stages of the digital receiver is shown in Figures B.3 and B.4.

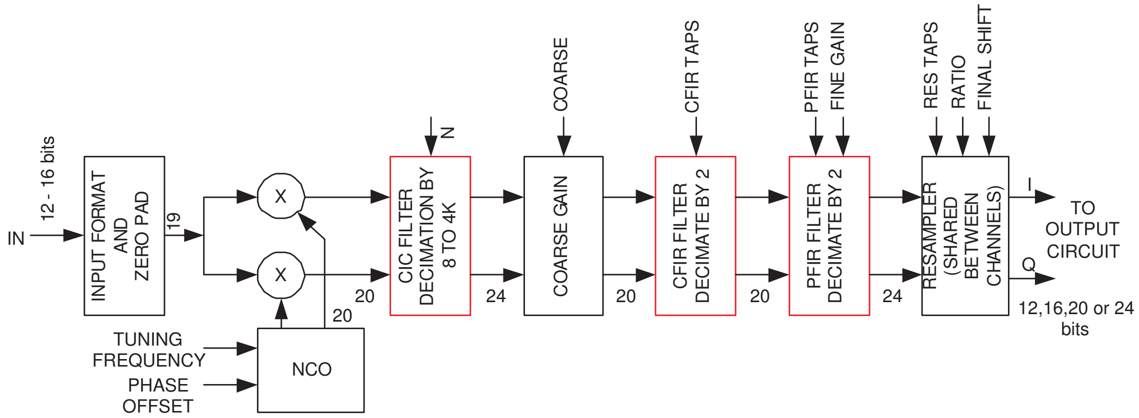

Figure B.2 – Functional diagram of one of the digital receiver modules of the receiver chip GC4016 inside the ECDR-GC214-PCI digital receiver card.

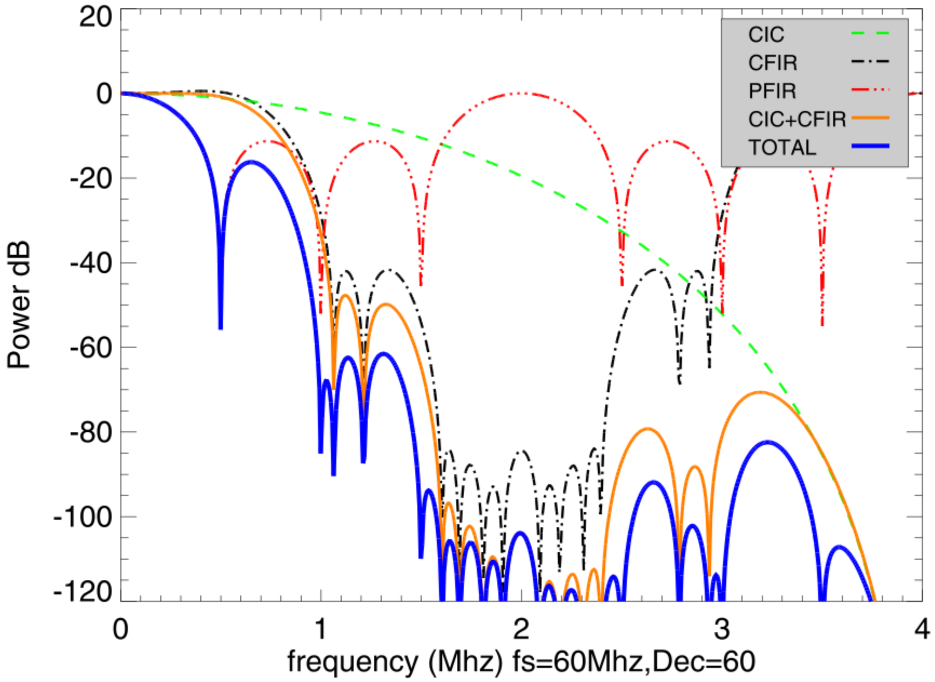

Figure B.3 – Frequency response of the digital receiver configured as a matched filter for a rectangle transmitted pulse.

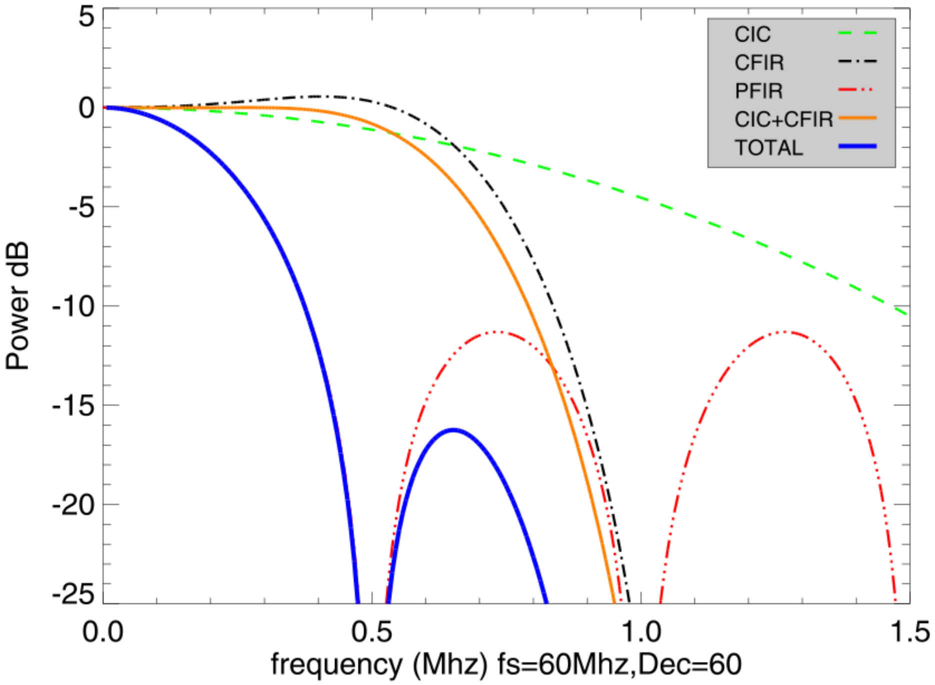

Figure B.4 – Detail of the frequency response of the digital receiver. Similar to Figure B.3 but zoomed in.

REFERENCES

Akgiray, A. H. (2007), Calibration of Jicamarca radar using F-region incoherent scatter for measurements of D-region backscatter RCS, Master's thesis, University of Illinois at Urbana-Champaign, Urbana, Illinois.

Bilitza, D. (2001), International Reference Ionosphere 2000, *Radio Science*, *36*(2), 261–275, doi:10.1029/2000RS002432.

Bougeret, J.-L., and M. Pick (2007), Solar radio emissions, in *Handbook of the Solar-Terrestrial Environment*, edited by Y. Kamide and A. Chian, handbook 6, pp. 133–151, Springer-Verlag, Berlin Heidelberg.

Bureau, R. (1939), Les renforcements de la propagation des ondes longues en coïncidence avec les évanouissements des ondes courtes; leur observation par l'enregistrement des parasites atmosphériques, *Journal de Physique et le Radium*, *10*(6), 260–270, doi:10.1051/jphysrad:01939001006026000.

Carrington, R. C. (1859), Description of a singular appearance seen in the sun on September 1, 1859, *Monthly Notices of the Royal Astronomical Society*, *20*, 13–15.

Chau, J. L., and R. F. Woodman (2004), Daytime vertical and zonal velocities from 150-km echoes: Their relevance to F-region dynamics, *Geophysical Research Letters*, *31*(L17801), 1–4, doi:10.1029/2004GL020800.

Cliver, E. W. (2001), Solar flare classification, in *Encyclopedia of Astronomy and Astrophysics*, edited by P. Murdin, 2285, pp. 1–4, Institute of Physics Publishing, Bristol, UK, doi:10.1888/0333750888/2285.

Davies, K. (1969), *Ionospheric Radio Waves*, 1 ed., Blaisdell Publishing Company, Waltham, MA.

Dellinger, J. H. (1937), Sudden ionospheric disturbances, *Terrestrial Magnetism and Atmospheric Electricity*, *42*(1), 49–53, doi:10.1029/TE042i001p00049.

Farley, D. T. (2009), The equatorial E-region and its plasma instabilities: a tutorial, *Annales Geophysicae*, *27*(4), 1509–1520.

Fritts, D. C., L. Yuan, M. H. Hitchman, L. Coy, E. Kudeki, and R. F. Woodman (1992), Dynamics of the equatorial mesosphere observed using the Jicamarca MST radar during June and August 1987, *Journal of Atmospheric Sciences*, *49*(24), 2353–2371, doi:10.1175/1520-0469(1992)049<2353:DOTEMO>2.0.CO;2.

Hargreaves, J. K. (1979), *The upper atmosphere and solar-terrestrial relations : an introduction to the aerospace environment*, Van Nostrand Reinhold, New York, NY.

Hargreaves, J. K. (1992), *The solar-terrestrial environment: , An introduction to geospace - the science of the terrestrial, upper atmosphere, ionosphere and magnetosphere.*, Cambridge Atmospheric and Space Science Series (5), 1 ed., Cambridge University Press.

Hedin, A. E. (1991), Extension of the MSIS thermosphere model into the middle and lower atmosphere, *Journal of Geophysical Research*, *96*(A2), 1159–1172, doi:10.1029/90JA02125.

Kane, S. R. (1974), Impulsive (flash) phase of solar flares: Hard X-ray, microwave, EUV and optical observations, in *Coronal Disturbances*, edited by G. J. Newkirk, 57, pp. 105–141, IAU symposium, Boston, MA.

Koskinen, H. E. J. (2011), *Physics of Space Storms From the Solar Surface to the Earth*, 1 ed., Springer, doi:10.1007/978-3-642-00319-6.

Kudeki, E. (2006), *Lecture notes on Applications of Radiowave Propagation*, Department of Electrical and Computer Engineering at the University of Illinois at Urbana-Champaign, Urbana, Illinois.

Kudeki, E., and C. D. Fawcett (1993), High resolution observations of 150 km echoes at Jicamarca, *Geophysical Research Letters*, *20*(18), 1987–1990, doi:10.1029/93GL01256.

Kudeki, E., and M. A. Milla (2011), Incoherent scatter spectral theories–Part I: A general framework and results for small magnetic aspect angles, *IEEE Transactions on Geoscience and Remote Sensing*, *49*(1), 315–328, doi:10.1109/TGRS.2010.2057252.

Lang, K. R. (2000), *The Sun from Space*, Springer, Berlin, Germany.

Lehmacher, G. A., E. Kudeki, A. H. Akgiray, L. Guo, P. M. Reyes, and J. L. Chau (2009), Radar cross sections for mesospheric echoes at Jicamarca, *Annales Geophysicae*, *27*(7), 2675–2684.

Levanon, N. (1988), *Radar Principles*, Wiley-Interscience, New York, NY.

Milla, M. A., and E. Kudeki (2006), F-region electron density and T_e/T_i measurements using incoherent scatter power data collected at ALTAIR, *Annales Geophysicae*, *24*(5), 1333–1342.

Milla, M. A., and E. Kudeki (2011), Incoherent scatter spectral theories–Part II: Modeling the spectrum for modes propagating perpendicular to $\vec{B}$, *IEEE Transactions on Geoscience and Remote Sensing*, *49*(1), 329–345, doi:10.1109/TGRS.2010.2057253.

Ochs, G. R. (1965), The large 50 mc/s dipole array at Jicamarca radar observatory, *NBS Report 8772*, National Bureau of Standards, 1965.

Primdahl, F. (1979), The fluxgate magnetometer, *Journal of Physics E: Scientific Instruments*, *12*(4), 241–253, doi:10.1088/0022-3735/12/4/001.

Prölss, G. W. (2004), *Physics of the Earth's Space Environment, An Introduction*, 1 ed., Springer Berlin / Heidelberg.

Rastogi, P. K., J. D. Mathews, W.-P. Ying, and J. Rottger (1988), Simultaneous VHF and UHF radar observations of the mesosphere at Arecibo during a solar flare: A check on the gradient-mixing hypothesis, *Radio Science*, *23*(2), 97–105.

Reyes, P. M., M. A. Milla, E. Kudeki, G. A. Lehmacher, and J. L. Chau (2009), Study of the effects of solar flare events observed over Jicamarca in the MST-ISR campaigns, in *poster at CEDAR Workshop 2009*.

Rishbeth, H., and O. K. Garriott (1969), *Introduction to Ionospheric Physics*, *International Geophysics Series*, vol. 14, 1 ed., Academic Press, INC., New York, NY and London.

Volland, H. (1966), On the theory of the sudden enhancement of atmospherics (SEA), *Journal of Atmospheric and Terrestrial Physics*, *28*(4), 409–423, doi:10.1016/0021-9169(66)90096-1.

Wild, J. P., S. F. Smerd, and A. A. Weiss (1963), Solar bursts, *Annual Review of Astronomy and Astrophysics*, *1*, 291–366, doi:10.1146/annurev.aa.01.090163.001451.

Woodman, R. F., and A. Guillen (1974), Radar observations of winds and turbulence in the stratosphere and mesosphere, *Journal of the Atmospheric Sciences*, *31*(2), 493—505, doi:10.1175/1520-0469(1974)031<0493:ROOWAT>2.0.CO;2.